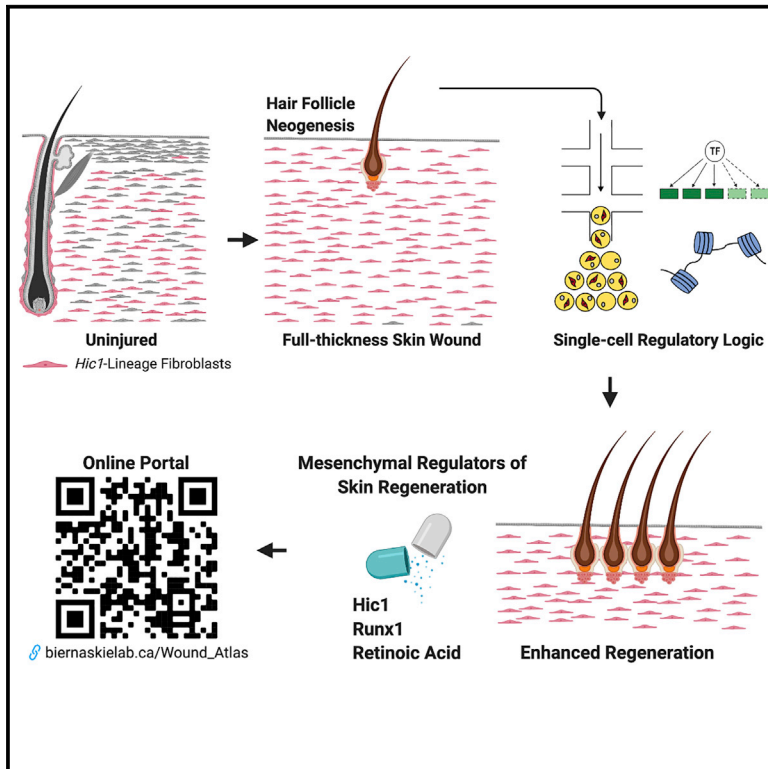


Distinct Regulatory Programs Control the Latent Regenerative Potential of Dermal Fibroblasts during Wound Healing

Graphical Abstract



Authors

Sepideh Abbasi, Sarthak Sinha, Elodie Labit, ..., Fabio M.V. Rossi, T. Michael Underhill, Jeff Biernaskie

Correspondence

jeff.biernaskie@ucalgary.ca

In Brief

Abbasi et al. show that interfollicular (but not hair follicle-associated) mesenchymal progenitors generate the bulk of reparative fibroblasts in skin wounds. Wound microenvironments remodel the regulatory landscape of recruited fibroblasts, resulting in regeneration centrally and scar-formation peripherally. Pharmacogenetic modulation of regeneration-associated regulators within wound-activated fibroblasts modifies healing outcomes.

Highlights

- Hair follicle (HF) dermal stem cells make minor contributions to skin and HF neogenesis
- Extrafollicular *Hic1*⁺ progenitors regenerate injured dermis and populate neogenic HFs
- Distinct transcriptional and epigenetic changes mediate fibroblast heterogeneity
- Runx1, retinoic acid, and *Hic1* control mesenchymal regenerative competence



Article

Distinct Regulatory Programs Control the Latent Regenerative Potential of Dermal Fibroblasts during Wound Healing

Sepideh Abbasi,^{1,5} Sarthak Sinha,^{1,5} Elodie Labit,^{1,5} Nicole L. Rosin,¹ Grace Yoon,¹ Waleed Rahmani,¹ Arzina Jaffer,¹ Nilesh Sharma,¹ Andrew Hagner,¹ Prajay Shah,¹ Rohit Arora,¹ Jessica Yoon,¹ Anowara Islam,¹ Aya Uchida,¹ Chih Kai Chang,² Jo Anne Stratton,¹ R. Wilder Scott,² Fabio M.V. Rossi,² T. Michael Underhill,² and Jeff Biernaskie^{1,3,4,6,*}

¹Department of Comparative Biology and Experimental Medicine, Faculty of Veterinary Medicine, University of Calgary, Calgary, AB T2N 4N1, Canada

²Biomedical Research Centre, University of British Columbia, Vancouver, BC, Canada

³Alberta Children's Hospital Research Institute, University of Calgary, Calgary, AB T2N 4N1, Canada

⁴Hotchkiss Brain Institute, Cumming School of Medicine, University of Calgary, Calgary, AB T2N 4N1, Canada

⁵These authors contributed equally

⁶Lead Contact

*Correspondence: jeff.biernaskie@ucalgary.ca

<https://doi.org/10.1016/j.stem.2020.07.008>

SUMMARY

Dermal fibroblasts exhibit considerable heterogeneity during homeostasis and in response to injury. Defining lineage origins of reparative fibroblasts and regulatory programs that drive fibrosis or, conversely, promote regeneration will be essential for improving healing outcomes. Using complementary fate-mapping approaches, we show that hair follicle mesenchymal progenitors make limited contributions to wound repair. In contrast, extrafollicular progenitors marked by the quiescence-associated factor *Hic1* generated the bulk of reparative fibroblasts and exhibited functional divergence, mediating regeneration in the center of the wound neodermis and scar formation in the periphery. Single-cell RNA-seq revealed unique transcriptional, regulatory, and epithelial-mesenchymal crosstalk signatures that enabled mesenchymal competence for regeneration. Integration with scATAC-seq highlighted changes in chromatin accessibility within regeneration-associated loci. Finally, pharmacological modulation of *RUNX1* and retinoic acid signaling or genetic deletion of *Hic1* within wound-activated fibroblasts was sufficient to modulate healing outcomes, suggesting that reparative fibroblasts have latent but modifiable regenerative capacity.

INTRODUCTION

Following deep skin injury, mammalian evolution has selected for accelerated wound closure at the expense of generating a fibrotic scar. Our inability to regenerate functional dermis and the appendages contained within it is a primary impediment to human skin wound healing (Eming et al., 2014).

Intriguingly, however, some capacity for tissue regeneration, including new hair follicle (HF) formation following full-thickness excisional skin wounds, has been demonstrated in mice (Ito et al., 2007; Fan et al., 2011; Seifert et al., 2012), serving as a powerful model to understand the mechanisms underlying skin regeneration. The epithelial component of neogenic HFs derives from emigrating extrafollicular *Lgr5*/*Lgr6*⁺ epithelial progenitors that reconstitute a new stem cell niche and resume cyclic regenerative function (Ito et al., 2007; Wang et al., 2017). The source of dermal regeneration remains unknown. Typically, neodermal repair in mammals involves formation of a fibrotic scar because of a predominance of incoming dermal fibroblasts predisposed to excessive production of fibrillar extracellular matrix (Driskell

et al., 2013; Rinkevich et al., 2015). Thus, determining the origin of fibroblasts that comprise the specialized mesenchymal cells that instruct HF neogenesis and how injury-mobilized fibroblasts evade adoption of fibrotic phenotypes and, conversely, acquire regenerative mesenchymal competence will be critical to enable therapies designed to improve wound healing outcomes.

The HF has long been postulated to be a potential source of regenerative mesenchymal cells during wound healing (Jahoda and Reynolds, 2001). Indeed, endogenous bipotent dermal stem cells residing within adult HFs (hfDSCs) function to continuously repopulate HFs with new mesenchymal cells as they undergo repeated cycles of degeneration, remodeling, and regeneration (Rahmani et al., 2014). Here we first wanted to find out whether HF-associated mesenchymal progenitors participate in wound healing and whether they represent a primary source of inductive mesenchyme within neogenic HFs. We found that hfDSCs are mobilized following injury and migrate into wounds where they generate a small subset of fibroblasts but, contrary to our hypothesis, contribute only a minority of cells to neogenic HFs. In contrast, complementary fate mapping of both hfDSCs



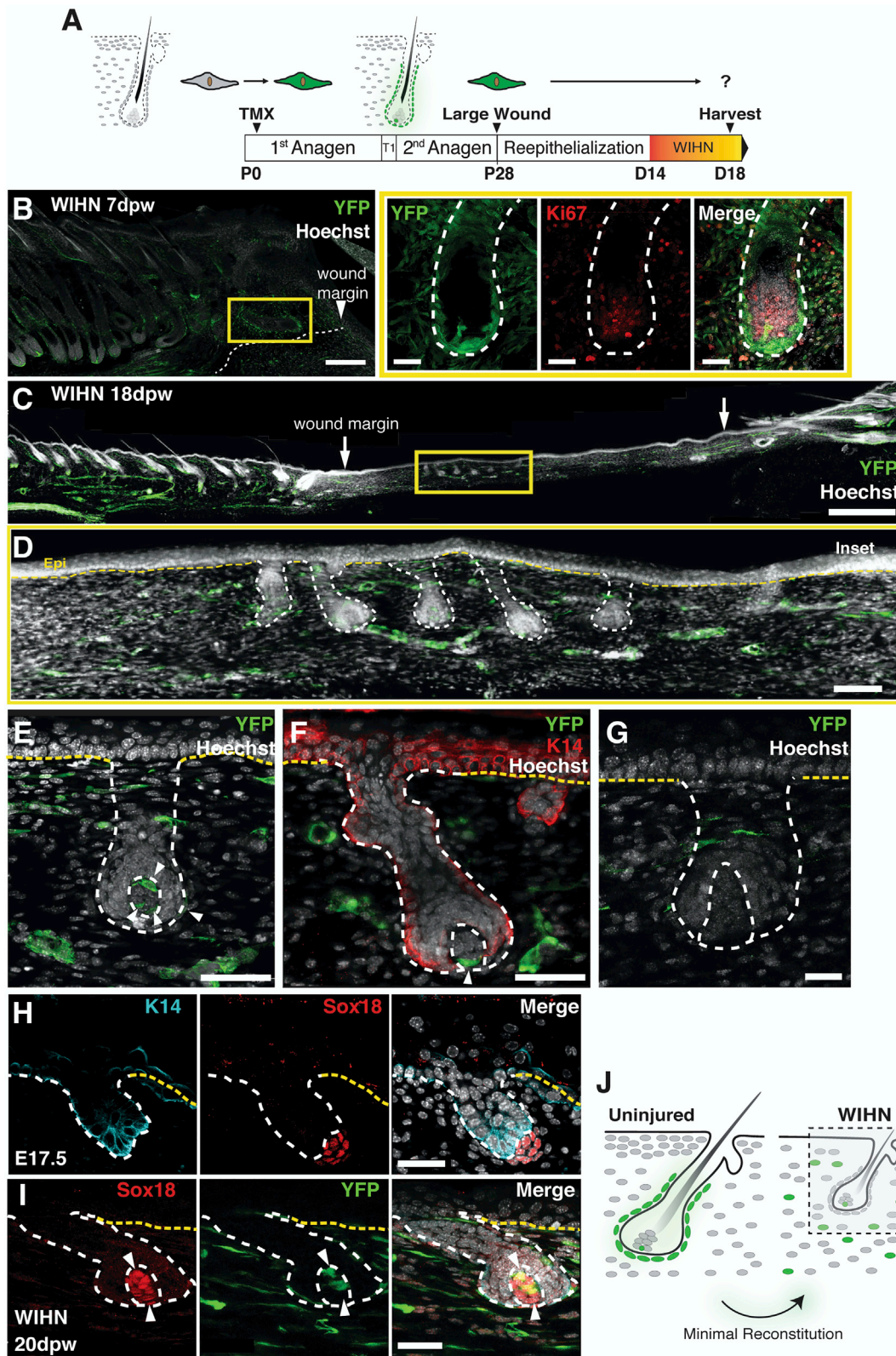


Figure 1. Inductive Mesenchyme within Neogenic Follicles Is Partly Reconstituted from Resident hfDSCs and Their Progeny

(A) Experimental timeline for fate-mapping experiments performed using α SMA-YFP mice, labeling hfDSCs and their progeny.

(B) YFP⁺ cells in HF along the wound margin delaminate from the outer root sheath, proliferate (Ki67, red), and migrate into healing wounds to contribute to dermal repair.

(legend continued on next page)

and extrafollicular mesenchymal progenitors using the quiescence-associated factor hypermethylated in cancer 1 (*Hic1*) demonstrated robust contribution to wound neoderms and more than 90% reconstitution of inductive mesenchyme within neogenic follicles. Single-cell RNA sequencing and ATAC-seq, revealed that discrete wound microenvironments activate unique transcriptional, regulatory, and epigenetic programs within mobilized extrafollicular fibroblasts, leading to acquisition of mesenchymal regenerative competence to support skin regeneration.

RESULTS

hfDSC Progeny Are Minor Contributors to Neogenic HFs

To determine whether hfDSCs and their progeny contribute to dermal repair or regeneration, we took advantage of α SMA^{CreERT2}:Rosa^{YFP} (α SMA-YFP) mice that faithfully mark hfDSCs and their progeny located in the DS (dermal sheath) and DP (dermal papilla) (Rahmani et al., 2014; Shin et al., 2020) but not interfollicular fibroblasts during homeostasis. Tamoxifen was administered to neonatal α SMA-YFP mice to label the hfDSC lineage, marking nearly all HFs (~30 YFP⁺ DS cells and ~5 YFP⁺ hfDSCs in each HF) (González et al., 2017). Mice received large full-thickness skin wounds at 28 days of age (Figure 1A), as described previously (Ito et al., 2007). Following injury, there was an increased density of YFP⁺ cells at the margins of the wound, particularly surrounding the lower half of HFs (Figure 1B), suggesting progressive delamination and migration of hfDSCs and their progeny from wound margins toward the lesion center, where wound-induced HF neogenesis (WIHN) is typically observed. Indeed, wounds in α SMA-YFP mice contained neogenic HF pegs by 18–20 days post wounding (dpw) (Figures 1C and 1D), and a few YFP⁺ hfDSC progenies had integrated into the DP and DS of nascent hair pegs (Figures 1E and 1F). Although many neogenic HFs contained α SMA-YFP⁺ cells, we also observed ~10% of HFs in which YFP⁺ cells were entirely absent (Figure 1G). Because neogenic HFs morphologically resemble embryonic HFs (Ito et al., 2007), we wanted to find out whether YFP⁺ hfDSC progeny incorporating into neogenic follicles recapitulate features of embryonic mesenchyme. Immunostaining for Sox18, which is exclusively expressed in dermal condensate/DP of all hair types during HF morphogenesis (Figure 1H; Pennisi et al., 2000), revealed discrete reactivation of Sox18 in the DP of new HFs (Figure 1I). In contrast, Sox18 expression remained absent in pre-existing HFs surrounding the wound (data not shown).

Neogenic HFs enter second anagen around 45 dpw (Wang et al., 2015). To evaluate the fate of mesenchymal populations within *de novo* HFs in second anagen and later regenerative cycles, we harvested large wounds at 60, 77, 90, and 140 dpw (Figures S1A–S1H). We compared the frequency of YFP⁺ HFs, DS, and DP from the second or later hair cycles with the first cycle

(18–30 dpw). Our analysis showed that 100% of regenerated HFs contained at least one YFP⁺ cell after 2 or more HF cycles, which increased compared with the first cycle (91.83% ± 4.1%; Figure S1I). The frequency of HFs with YFP⁺ DS remained consistent over successive hair cycles (90.17 ± 3.57 versus 90.92 ± 5.43, $p > 0.5$, first hair cycle versus two or more regenerative cycles, respectively; Figure S1J). Moreover, the frequency of YFP⁺ DP also increased over multiple hair cycles, from 76.11 ± 9.802 in the first cycle to 88.54 ± 3.59 in the subsequent cycles ($p > 0.5$; Figure S1K). To examine the fate of YFP⁺ DP cells over multiple cycles, we quantified the percentage of YFP⁺ DP cells in regenerated HFs and found that YFP⁺ hfDSCs maintained their capacity to populate the DP over consecutive hair cycles (Figure S1L). Intriguingly, when neogenic HFs transitioned to telogen, a subset of telogen DP retained YFP⁺ cells (Figures S1C and S1D). In uninjured skin, hfDSCs (and their labeled progeny) redistribute to the periphery of telogen DP and do not remain in telogen DP (Rahmani et al., 2014). Also, over multiple anagen cycles, (~90 dpw), YFP⁺ cells colonizing neogenic HFs exhibited long-term retention and a successive capacity to repopulate DP and DS, similar to hfDSCs in adult skin (Figures S1G and S1H).

These findings demonstrate that, although hfDSC progeny can reactivate WIHN-associated transcriptional programs, they are not the primary contributors to dermal wound healing and neogenic HFs (Figure 1J). Their overall contribution to regeneration was limited, considering that many neogenic HFs did not contain any labeled cells and that more than 75% of mesenchymal cells comprising each neogenic HF (DP and DS) were α SMA-YFP⁻ (Figures S1B and S1E–S1I). Labeled and unlabeled fibroblasts incorporated into neogenic HFs and generated *bona fide* DP/DS cells to support sustained HF regeneration. Moreover, injury-mobilized fibroblasts appeared to re-establish an equivalent hfDSC population, successively regenerating the DS over consecutive cycles (Figure S1). Together, this suggests that follicle-associated mesenchymal cells play only a modest role in dermal repair and WIHN and that the vast majority of neoderms regeneration and WIHN is carried out by extrafollicular dermal progenitors/fibroblasts.

Hic1-Lineage-Comprising HFs and Extrafollicular Fibroblasts Support HF Regeneration within Permissive Microenvironments

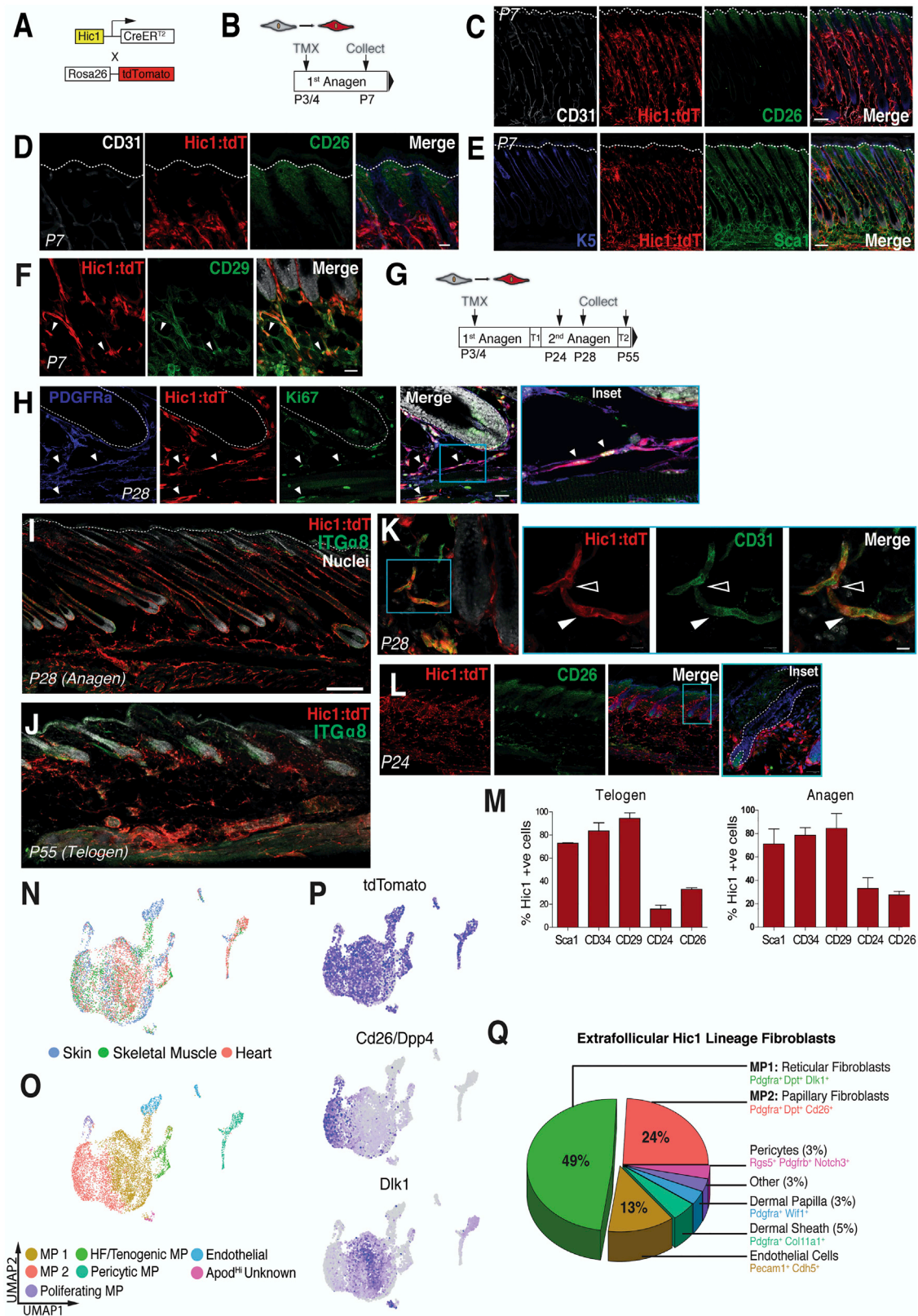
Because hfDSCs made only modest contributions to neogenic HFs, we set out to determine the origin of the remaining regenerative mesenchyme. Recent studies have uncovered a pool of mesenchymal progenitors (MPs) resident within skeletal muscle (Scott et al., 2019) and the heart (Soliman et al., 2020) that are marked by their expression of *Hypermethylated in Cancer 1* (*Hic1*) and activated following tissue injury. Our own previous single-cell RNA sequencing (scRNA-seq) characterization of aged HFs identified *Hic1* expression in the HF mesenchyme and

(C–G) By 18 days post-wounding (dpw), most neogenic follicles in the wound (C and D) contain hfDSC progeny (green) within the DP (E) and DS (F), but there is no contribution to epithelium (Keratin-14, red, F), whereas a subset of neogenic follicles are devoid of hfDSC progeny (G).

(H and I) Sox18 is uniquely expressed in the DP of developing (embryonic day 17 [E17]) HFs (H) and is similarly activated in hfDSC progeny (green), comprising the neogenic DP during WIHN (white, I).

(J) Schematic depicting hfDSC progeny as minor contributors to neogenic HFs.

Scale bars represent 500 μ m (C), 200 μ m (D), 50 μ m (E–G), and 30 μ m (H and I). The images in (B)–(D) are tiled and stitched.



(legend on next page)

enrichment for *Hic1* gene regulatory network activity within hfDSCs (Shin et al., 2020). Hence, we surmised that *Hic1* might similarly mark a conserved pool of MPs within adult mammalian skin. To test this, we first wanted to find out which cells in neonatal and adult skin express *Hic1*. Our short-term lineage trace (tamoxifen [TAM] induction at post-natal day 3 (P3)/P4, harvest at P7) using *Hic1*^{CreERT2};Rosa^{tdTomato} mice (or *Hic1*-tdT) (Figures 2A and 2B) revealed that tdTomato⁺ cells were preferentially distributed within reticular dermis and a lesser number in papillary dermis (Figures 2C–2F). Interestingly, *Hic1*-expressing cells also reside within perivascular niches and co-express markers typically associated with fibro-adipogenic MPs, such as PDGFR α , SCA1 (Ly6a), and CD29 (Figures 2C–2F; Rivera-Gonzalez et al., 2016; Shook et al., 2018; Soliman et al., 2020). To assess whether *Hic1*-expressing cells represent skin MPs, we wanted to determine whether (1) *Hic1* marked hfDSCs by performing long-term pulse-chase experiments over several HF cycles and assessed retention of *Hic1*-tdT⁺ cells in the hfDSC niche, (2) extrafollicular *Hic1*-lineage cells (comprising *Hic1*-expressing MPs and their fibroblast progeny) proliferate to supply new dermal cells during anagen, and (3) *Hic1*-lineage cells bear molecular resemblance to skeletal muscle and cardiac MPs.

First, short-term fate mapping using *Hic1*-tdT mice in which TAM was either administered during second anagen (P25; Figure S2A, S2C, S2D, S2F, and S2G) or second telogen (P55; Figure 2E) and skin was harvested 3 days later revealed *Hic1*-tdT⁺ cells in the HF dermal cup where hfDSCs reside. Indeed, we observed high concordance between *Hic1* mRNA and tdTomato reporter expression (Figure 2C) and undetectable spontaneous recombination (data not shown), validating use of this strain. To test whether *Hic1* marked hfDSCs, we performed long-term lineage tracing that extended over two HF cycles (Figures S2H–S2K) and found that *Hic1*-tdT⁺ cells were retained in the dermal cup during telogen over successive cycles (Figures S2I and S2K) and repopulated DS and DP in anagen (Figure S2J), exhibiting self-renewal and bipotent reconstitution of HF mesenchyme, as originally described for hfDSCs (Rahmani et al., 2014). Thus, *Hic1* marks at least a subset of hfDSCs. In addition, the *Hic1* lineage also marked perifollicular adipocytes (Figures S2M and S2N) but not the *arrector pili* muscles (Figure S2I).

Second, long-term fate mapping of interfollicular *Hic1*-lineage cells (P3/P4 TAM induction, P28 harvest) revealed that a subset was mitotically active in anagen (Figure 2H) and was preferentially located in the reticular dermis (Figures 2I–2L), as observed in our short-term trace (Figures 2A–2F). Interestingly, this ho-

meostatic activation of *Hic1*-expressing skin MPs to support the anagen-associated increase in HF and extrafollicular mesenchyme is unique to skin MPs because skeletal muscle and cardiac MPs remain in quiescence until challenged with an insult. In fact, damage-free activation of cardiac MPs leads to fibrofatty deposits within the myocardium, leading to arrhythmogenic cardiomyopathy (Soliman et al., 2020).

We then performed a molecular comparison of *Hic1*-lineage skin MPs with muscle and heart fibro-adipogenic MPs. Indeed, *Hic1*-lineage skin MPs co-expressed *Pdgfra*, *Ly6a* (SCA-1), and *Cd29* (Figure 2M). Integration of single-cell transcriptomes of *Hic1*-tdT⁺ cells isolated from intact skeletal muscle (GSM2976778), the heart (GSM4216418), and skin (GSM2910020) revealed striking similarities conserved across progenitor pools (Figures 2N–2P). Two distinct and conserved sub-clusters emerged from this analysis: *Mgp*⁺, *Dlk1*⁺, extracellular matrix (ECM)-rich reticular MP1 (annotated FAP1 by Scott et al., 2019), and *Cd26*⁺/*Dpp4*⁺, *Wnt2*⁺ papillary MP2 (annotated FAP2). Consistent with the *in vivo* characterization above, scRNA-seq-based quantifications confirmed that the *Hic1* lineage comprises HF (8%) and extrafollicular (73%) fibroblasts that preferentially reside within reticular dermal niches (49% reticular versus 24% papillary fibroblasts) (Figure 2Q).

Extrafollicular *Hic1*-Lineage Fibroblasts Are the Primary Contributors to Dermal Regeneration and WIHN

To determine whether *Hic1*-lineage skin MPs (encompassing hfDSCs and extrafollicular fibroblasts) and their progeny represent the origin of regenerative fibroblasts during WIHN, we created large full-thickness excision wounds in *Hic1*-tdT mice (4 weeks post-TAM labeling; Figure 3A). *Hic1*-tdT⁺ cells contributed to the vast majority of cells comprising the wound neodermis (Figure 3B). Upon inspection of neogenic follicles within large wounds, we discovered that at hair peg/germ stage, more than 90% of neogenic DP cells within each newly formed follicle (18–20 dpw) originated from the *Hic1*-tdT⁺ lineage (Figures 3B and 3C). Indeed, *Hic1*-tdT⁺ cells in neogenic DP upregulated the embryonic DP marker *Sox18* (Figure 3D), suggesting that local signals within the epicenter of the wound or via interaction with overlying epidermal basal cells initiated molecular processes that recapitulated skin morphogenesis. This was in stark contrast to the limited contribution shown by hfDSC-lineage cells alone (90.50% \pm 1.228% versus 19.34% \pm 1.95%, $p < 0.0001$; Figure 3E), indicating that extrafollicular *Hic1*-tdT⁺ fibroblasts are the primary source of mesenchymal cells within neogenic HFs. Next we wanted to find out whether *Hic1*-tdT⁺ cells

Figure 2. *Hic1* Lineage Marks Extra-Follicular Fibroblasts Closely Resembling Mesenchymal Progenitors (MPs) from Other Tissues

(A–F) Short-term fate mapping using *Hic1*^{CreERT2};Rosa^{tdTomato} (*Hic1*:tdT) mice (A) during first anagen (P7, B) revealed that *Hic1*:tdT⁺ cells preferentially reside within perivascular (C) and reticular dermal niches (D–F). *Hic1*:tdT⁺ cells (red) stained for the endothelial marker CD31 (white, C and D), the papillary fibroblast marker CD26 (green, C and D), the reticular fibroblast/progenitor marker *Sca1* (green, E), and CD29 (green, F).

(G–M) Long-term fate mapping of *Hic1*-expressing MPs labeled at P3–P4 and harvested at second anagen (P28) and telogen (P55) revealed *Hic1* lineage marks MPs residing within perivascular and reticular dermal niches.

(H) Immunostaining for Ki67 (green) showing co-localization with a subset of *Hic1*:tdT⁺ reticular dermis during early anagen.

(I–L) *Hic1*:tdT⁺ cells (red) co-stained for ITGA8 (green, I and J), CD31 (green, K), and CD26 (green, L) in second anagen (I, K, and L) and telogen (J).

(M) Flow cytometry analysis of *Hic1*:tdT⁺ cells in telogen and anagen skin.

(N and O) Integration of single-cell transcriptome profiles of *Hic1*-lineage MPs, colored by tissue of origin (N) and cell types and states (O).

(P) Two distinct MP states can be distinguished by the papillary dermal marker *Cd26/Dpp4* and the reticular dermal marker *Dlk1*.

(Q) scRNA-seq-based quantification of *Hic1*:tdT⁺ lineage composition at P28 anagen.

The images in (C), (E), (I), and (J) are tiled and stitched.

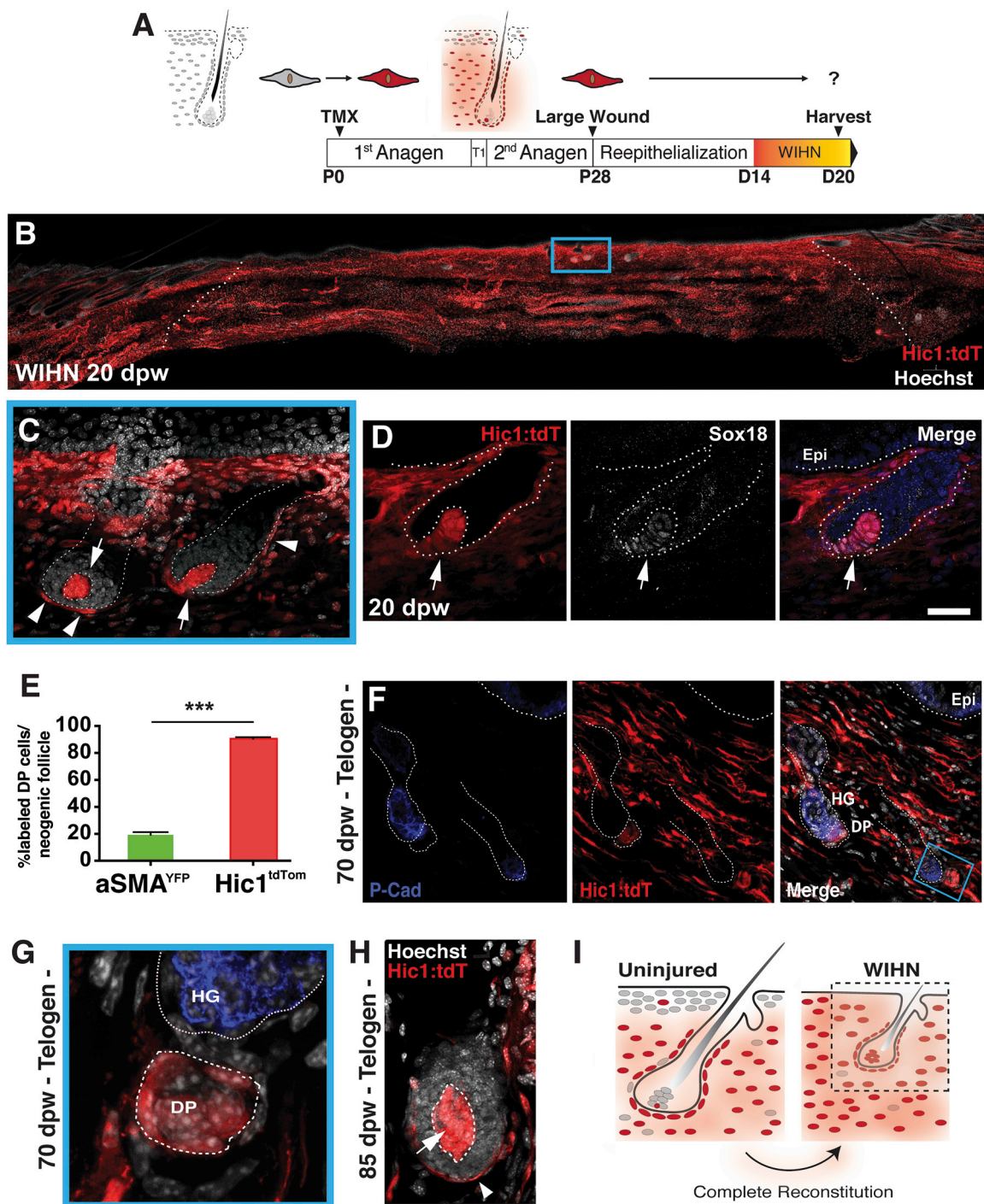


Figure 3. *Hic1*-Lineage Progenitors Repopulate the Injured Dermis and Reconstitute the Mesenchyme of Neogenic Follicles

(A) Experimental timeline for fate-mapping experiments performed using *Hic1*^{CreERT2}; *Rosa*^{tdTomato} mice labeling hfDSCs and extra-follicular progenitors.

(B) *Hic1*:tdT⁺ cells following large skin wounds at P28 anagen harvested 20 dpw.

(C) Inset (blue box in A) showing magnified neogenic HF within the wound. *Hic1*:tdT⁺ cells (red) reconstitute DP (arrow) and DS (arrowheads).

(D) *Hic1*:tdT⁺ cells (red) within the neogenic DP reactivate Sox18 (white).

(E) Comparison of inductive DP reconstitution capacity in hfDSC lineage cells (α SMA:YFP⁺) versus the combination of hfDSCs and extra-follicular progenitors (*Hic1*:tdT⁺). *n* = 5 mice from each group with 10–45 HF analyzed per mouse; ****p* < 0.0001 (t test), *df* = 71.

(F) Telogen HF at 70 dpw show retention of *Hic1*:tdT⁺ cells (red) in resting DP. Hair germ is stained with p-cadherin (blue).

(G) High-magnification inset from (F).

(legend continued on next page)

provide sustained inductive function and could reconstitute the HF mesenchyme over consecutive hair cycles. To do this, wounds were collected at 70 and 85 dpw, allowing HFs to undergo at least two regenerative cycles. At 70 dpw, when the neogenic HFs are in telogen, almost all DP cells were *Hic1*:tdT⁺ (Figures 3F and 3G). Similarly, at 85 dpw, when neogenic follicles re-entered anagen, we found that the anagen DP was almost entirely comprised of *Hic1*-tdT⁺ cells (Figure 3H). In summary, extrafollicular *Hic1*-tdT⁺ fibroblasts demonstrated a robust contribution to neoderms and more than 90% reconstitution of inductive mesenchyme within neogenic HFs (Figure 3I). Importantly, similar levels of reconstitution by *Hic1*-lineage cells was observed following small wounds (Figure S3A). Also, because it has been recently that injury-responsive myofibroblasts can undergo myofibroblast-to-adipocyte transformations to generate new fat around neogenic follicles (Plikus et al., 2017), we wanted to find out whether *Hic1*-tdT⁺ myofibroblasts exhibited similar plasticity. Lineage tracing of *Hic1*-tdT⁺ cells extended to more than 60 days post-injury revealed that *Hic1*-tdT⁺ cells express the adipocyte marker perilipin (Figures S3B and S3C).

To further confirm the capacity of extrafollicular *Hic1*-lineage cells to reconstitute the HF niche and instruct epithelial cells to generate new HFs, we prospectively isolated *Hic1*-tdT⁻ cells from adult anagen skin and partitioned them into HF-associated and non-HF populations (Figures S3D and S3E). HF-associated *Hic1*-tdT⁺ cells were identified by expression of *Cd133* or *Itga9* (both indicative of DP) and *Itga8*⁺ or *Cd200*⁺ cells (indicative of DS) (Figure S3F). Each population was then combined with neonatal epithelial cells and transplanted into immune-deficient mice to assess their capacity to induce HF formation when provided with a permissive environment (Zheng et al., 2005; Biernaskie et al., 2009). Epithelial cells alone and epithelial cells combined with *Hic1*-tdT⁻ cells showed only rare HF formation, and they were typically small and abnormally shaped (Figures S3G and S3H). Intriguingly, *Hic1*-tdT⁺ cells were capable of robust HF induction and reconstitution of all mesenchymal compartments within the newly formed HFs, irrespective of their prior association with a HF (Figures S3I–S3N). Together, these results establish that extrafollicular *Hic1*-lineage MPs generate fibroblasts that are recruited into large wounds, where they acquire functionally diverse fibroblast fates (including inductive DP, hfDSCs, and DS) and adipocytes to enable neodermal regeneration.

Single-Cell Transcriptomics Reveals that Distinct Molecular Programs Regulate Fibroblast Response to Injury

To dissect the molecular programs driving divergent fibroblast fates during fibrotic and regenerative healing, we profiled 29,269 single cells from uninjured skin (P28), small wounds at 8 and 14 dpw, and large wounds (divided into central and peripheral domains) at 14 dpw. To increase power for interrogating

fibroblast heterogeneity, *Hic1*:tdT⁺ and tdT⁻ cells were purified by fluorescence-activated cell sorting (FACS) to enrich fibroblasts and wound microenvironment-establishing cells, respectively, and profiled using the droplet-based 10x Genomics system (v.2 chemistry) (Zheng et al., 2017; Stratton et al., 2019b). We selected 12,326 *Hic1*-tdT⁺ fibroblasts based on *Pdgfra*, *Dpt*, and *tdTomato* expression (Figures S4A–S4C) and performed unsupervised clustering using t-distributed stochastic neighbor embedding (t-SNE) to assess transcriptional heterogeneity within fibroblasts isolated from different wound types (Figure S4D). Because most clusters contained fibroblasts from one wound type (and mixed clusters may have arisen from imprecise margin delineation across 2 pooled wounds), fibroblasts in the outlined clusters that met quality control gating were reclustered and colored according to wound type (Figure 4A).

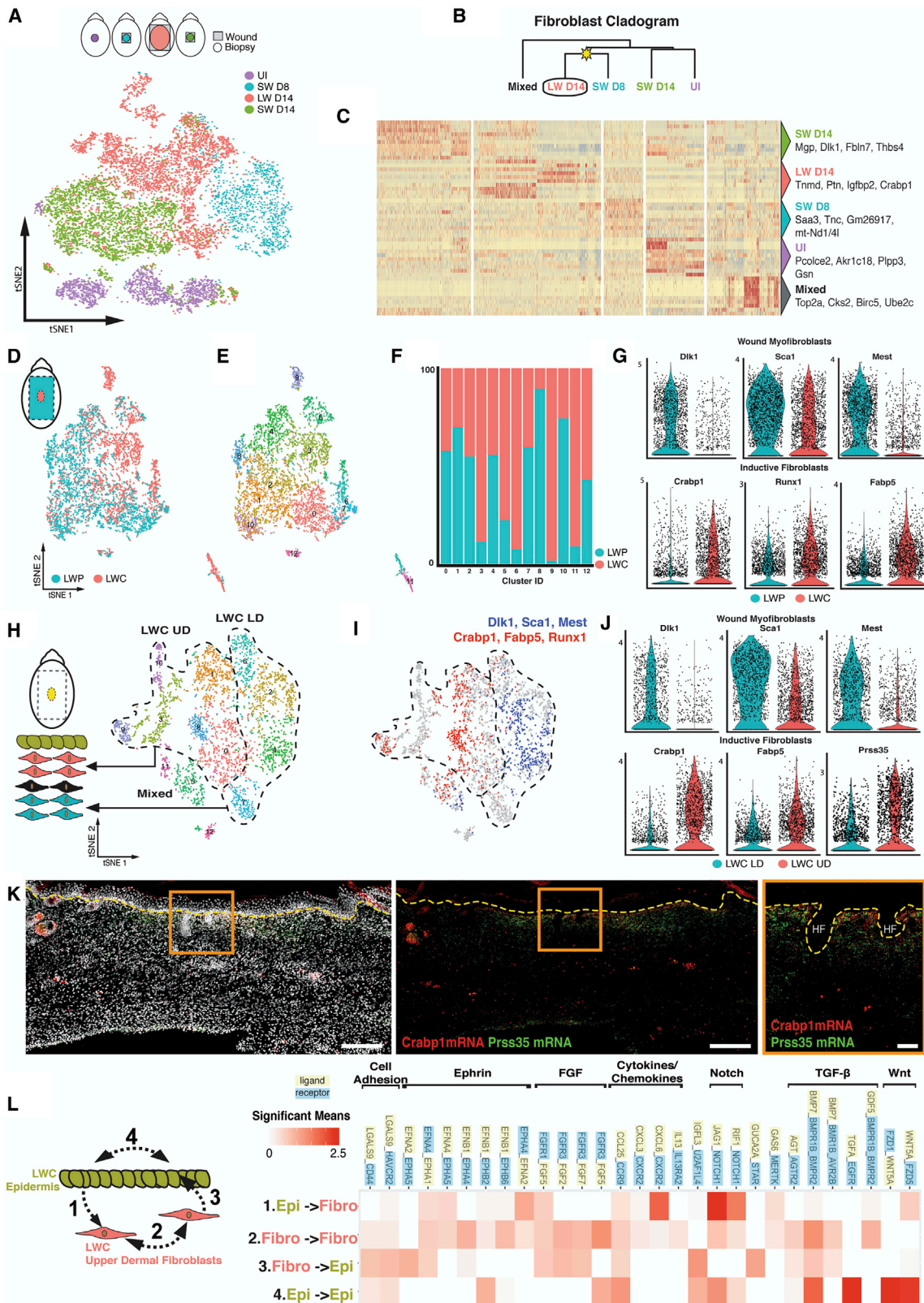
Next we examined the overall transcriptional relatedness of fibroblasts isolated from different wound types (Figure 4B) and found that, although an earlier wound stage-matched small wound (SW) is a better comparator for large wounds (LWs) 14 dpw, the overarching transcriptional landscape acquired by LW fibroblasts is quite distinct (Figures 4A–4C). To identify the wound-specific fibroblast transcriptional response, we calculated the difference in gene expression for each gene between fibroblasts in that wound sample and compared it with the average of fibroblast expression from all other wound types and uninjured skin. LW 14 dpw fibroblasts showed an overall enrichment of genes associated previously with specification of embryonic dermis, including *Crabp1*, *Tnmd*, *Ptn*, and *Igf2bp2* (Sennett et al., 2015; Budnick et al., 2016). To further dissect regional variation in fibroblasts recruited to central versus peripheral domains of LWs, we reclustered all LW 14 dpw fibroblasts and colored according to the wound region (Figure 4D) and cluster ID (Figure 4E). Unbiased determination of clusters was determined using the Louvain algorithm, and assignment of each cluster to either wound domain was quantitatively determined by percent cell distribution (Figures 4E and 4F). LW center (LWC) fibroblasts preferentially expressed cellular retinoid-binding proteins (i.e., *Crabp1* and *Fabp5*) and *Runx1*, whereas LW periphery (LWP) fibroblasts expressed scar-associated markers such as *Dlk1*, *Sca1*, and *Mest* (Guerrero-Juarez et al., 2019; Figure 4G). Intriguingly, acquisition of near-identical regenerative (i.e., *Crabp1*, *Prss35*, and *Fabp5*) and fibrotic (i.e., *Dlk1* and *Sca1*) programs in α SMA⁺ myofibroblasts within central and peripheral domains occurs much earlier than scar detachment/HF neogenesis (Figures S4H–S4J). This suggests that mesenchymal competence is established much earlier than neogenic events and is subsequently sustained for at least a 9-day window as *de novo* placodes continue to emerge until 19 dpw (Fan et al., 2011).

Because LWP fibroblasts shared a striking overlap with LWC fibroblasts at the gene expression level (Figure 4D), we reclustered LWC fibroblasts to subdivide them into regenerative LWC upper dermis (*Crabp1*, *Fabp5*, *Prss35*, and *Runx1*) and non-regenerative

(H) Anagen neogenic follicles at 85 days post-injury show a sustained presence of *Hic1*:tdT⁺ cells (red) within DP (arrow) and DS (arrowheads) over multiple hair cycles.

(I) Schematic depicting extrafollicular *Hic1*-lineage fibroblasts as the primary contributor to dermal regeneration and WIHN.

Nuclei are stained with Hoechst (white) in (C)–(H). Scale bars represent 200 μ m (B–D) and 30 μ m (F). The images in (B) are tiled and stitched. HF, hair follicle; DP, dermal papilla; hfDSC, hair follicle dermal stem cells; WIHN, wound-induces hair follicle neogenesis; df, degrees of freedom.



(legend on next page)

LWC (*Dlk1*, *Sca1*, and *Mest*) lower dermis, as described previously (Guerrero-Juarez et al., 2019; Figures 4H–4J). We spatially mapped LWC upper dermal fibroblasts by co-staining with *Crabp1* and *Prss35* RNAscope probes at 15 dpw (Figure 4K). Indeed, *Crabp1*⁺/*Prss35*⁺ fibroblasts localized within the upper, superficial neodermis (and were entirely absent from the deep neodermis) in wounds. This suggests that spatial segregation of fibroblasts and their interactions with overlying epidermal basal cells were necessary for acquisition of regenerative competence. Because epithelial-mesenchymal interaction between competent fibroblasts and epidermal stem cells initiates *de novo* HF formation in embryonic skin, we reasoned that similar regulatory interactions may establish regenerative competence to enable WIHN. Indeed, overlaying 14 dpw LWC upper dermal fibroblasts with LWC epidermal cells using CellPhoneDB (Vento-Tormo et al., 2018) revealed a unique interactome (compared with SWs 8 dpw; Figure S4E), reminiscent of signals exchanged during HF morphogenesis. For example, ephrin receptors (i.e., *Efn2*, *Efn4*, and *Efnb1*) and ligands (i.e., *Epha1*, *Epha4*, *Epha5*, *Ephb2*, and *Ephb6*), known to act as negative regulators of epidermal proliferation during embryonic skin morphogenesis (Genander, Holmberg and Frisén, 2010), were predicted to interact within the regenerative neodermis, suggesting that reactivation of conserved regulatory interactions enables mesenchymal competence for regeneration (Figure 4L).

Activation of Unique Gene-Regulatory Networks (GRNs) Underlies Regenerative Competence in Wound-Responsive Fibroblasts

To identify signaling networks that might confer regenerative or fibrotic fibroblast function, we first performed single-cell regulatory network inference and clustering (SCENIC) analysis (Aibar et al., 2017) on *Hic1*-lineage fibroblasts from LWs, SWs, and uninjured skin (Figures S5A–5E). Fibroblasts from SWs at 8 dpw showed the greatest similarity to LW 14 dpw fibroblasts, as revealed by hierarchical clustering using regulon (co-expressed target genes regulated by a transcription factor) activity. Intriguingly, although the transcriptional repressor of Hedgehog (Hh) signaling, *Glis2*, is active in SW 8 dpw fibroblasts, direct effectors of Hh signaling, such as *Gli1*, are active only in LWC 14 dpw fibroblasts (Figures S5A–S5D). This supports the view that Hh signaling downstream of β -catenin contributes to mesenchymal competence for regeneration of *de novo* HFs within interfollicular

epidermis (Silva-Vargas et al., 2005) and SWs (Lim et al., 2018). We also identified a set of 9 core regulons (*Xrcc4*, *Rab14*, *Bmyc*, *Mitf*, *Irf8*, *Klf5*, *Zic1*, *Gli1*, and *Etv1*) shared between the LWC 14 dpw and uninjured skin that have been implicated previously in acquisition of dermal condensate induction during HF morphogenesis (Rendl et al., 2005; Cadau et al., 2013) but were absent during fibrotic healing (Figure S5D).

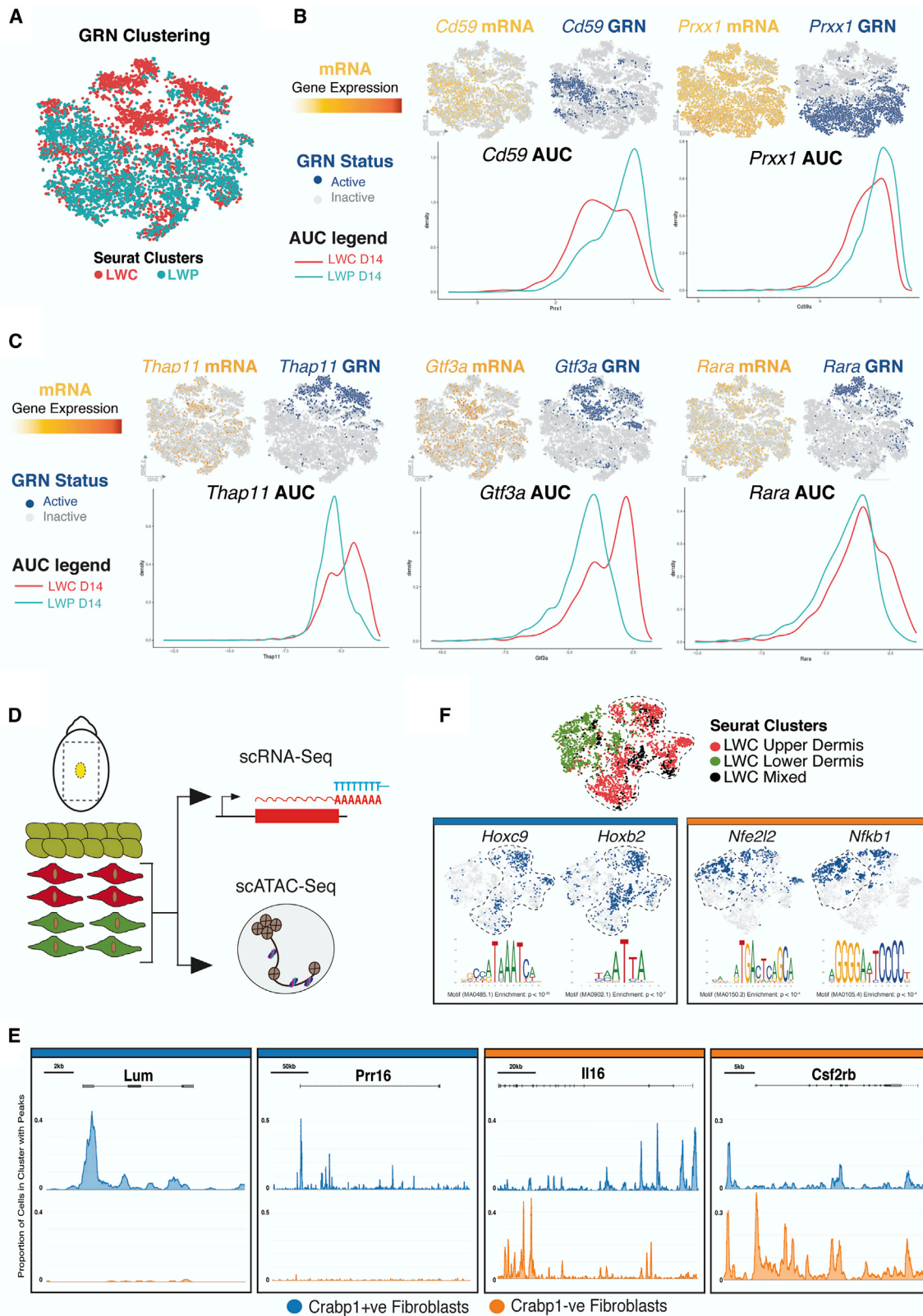
To dissect WIHN regulators active in a region-specific fashion, we performed t-SNE reduction using SCENIC's regulon matrix and annotated fibroblasts based on their location in LWs 14 dpw (LWC or LWP; Figures 5A–5C). Although transcription factors (TFs) such as *Cd59* and *Prx1* exhibited predictable patterns of transcript enrichment (yellow) paired with concomitant activation of downstream regulatory networks (blue) in LWP fibroblasts (Figure 5B), we observed highly discrepant TF network activity in LWC fibroblasts (Figure 5C). Notably, although LWC and LWP fibroblasts expressed comparable levels of *Thap11*, *Gt3a*, and *Rara* mRNA, this was not reflected by TF network activity because they were preferentially active (area under the curve [AUC]; Figures 5B and 5C) within LWC fibroblasts.

Acquisition of Hair-Inductive Capacity within Regeneration-Competent Fibroblasts

To further dissect transcriptional programs driving acquisition of a dermal condensate/DP state and the instructive signal that initiates epithelial proliferation and invagination within the LWC, we applied diffusion map (DM) analysis on LWC upper dermal fibroblasts (identified in Figure 4I). Because DM analysis reveals a phenotypic continuum by ordering cells based on transcriptional similarity (Haghverdi et al., 2016), we wanted to find out whether continuous transcriptional states connected inductive *Crabp1*⁺ LWC upper dermal fibroblasts to neogenic condensate cells. Interestingly, we observed a sequence of related transcriptional states that expressed markers associated with inductive mesenchyme (*Crabp1*), DS/hfDSCs (*S100a4* and *Cd200*) (Shin et al., 2020), and early dermal condensate/DP markers (*Rspo3* and *Sox18*), as confirmed by RNAscope (Figures 6A–6C). Overlaying *Rspo3*⁺ *Sox18*⁺ neogenic DP cells (Sennett et al., 2015; Joost et al., 2020) with *Wnt3*⁺ *Fgfr2*⁺ placode cells (Sennett et al., 2015) (captured in the *Hic1*-tdT⁺ fraction; data not shown) revealed receptor-ligand interactions (Figure 6D) that were distinct from LWC upper dermal fibroblasts with LWC epidermal cells

Figure 4. *Hic1*-Lineage Dermal Fibroblasts Are Recruited to Regenerative and Fibrotic Wounds and Exhibit Transcriptional and Functional Divergence

- (A) Unsupervised clustering of fibroblasts enriched in each wound projected on a t-SNE (determined by examining 12,326 fibroblasts in Figure S4D).
 (B) Hierarchical clustering by average gene expression.
 (C) Heatmap of top markers in each fibroblast subset.
 (D and E) LW fibroblasts subclustered and projected on a t-SNE; cells are colored by wound region (D) and cluster ID (clustering resolution, 0.6, E).
 (F) Relative contribution of LWC and LWP fibroblasts to each cluster.
 (G) Violin plots showing enrichment of myofibroblastic markers (*Dlk1*, *Sca1*, and *Mest*) in LWP clusters and, conversely, embryonic fibroblast markers (*Crabp1*, *Fabp5*, and *Runx1*) in LWC clusters. The y axis is on a log scale. Clusters are classified as being enriched for one sample type when more than 70% of fibroblasts in that cluster originated from any one sample.
 (H–J) Subclustering fibroblasts from LWC 14 dpw reveals two subpopulations, each comprising several clusters (clustering resolution, 0.6, H), distinguished by expression of myofibroblast or embryonic fibroblast markers (I and J). The *Dlk1*^{hi} *Sca1*^{hi} *Mest*^{hi} population is termed “lower dermal fibroblast,” *Crabp1*^{hi} *Fabp5*^{hi} *Prss35*^{hi} is termed “upper dermal fibroblast,” and clusters containing a mixture of the two gene sets are termed “mixed.”
 (K) Spatial distribution of upper dermal fibroblasts within wound neodermis was confirmed with RNAscope for *Crabp1* (red) and *Prss35* (green).
 (L) Divergent epithelial (green)-mesenchymal (pink) crosstalk initiated by upper dermal fibroblast in LWC 14 dpw compared with SW 8 dpw (Figure S4E). Ligands are shown in yellow and receptors in blue.
 The images in (K) are tiled and stitched. UI, uninjured; SW, small wound; LW, large wound; LWC, LW center.



(legend on next page)

(Figure 4L). Notably, we inferred the retinoic acid-inducible growth factor Midkine (Mdk) being secreted by neogenic DP cells that activate *Lrp1* or *Ptprz1* receptors in epithelial placodes (Figure 6D). Because Mdk is a confirmed secreted DP signal (Rendl et al., 2005) and a direct product of a retinoic acid-responsive gene (Muramatsu, 1993), it suggests that unique patterns of gene regulatory network activation are engaged within regenerative fibroblasts to enact distinct transcriptional and functional states associated with inductive capacity.

Because HF induction is exclusive to LWC upper dermal fibroblasts, we surmised that fibroblasts in the LWC activated at least two distinct sets of regulatory programs. One set imprinted regenerative plasticity within upper fibroblasts, whereas the other set enacted a scar forming phenotype within lower fibroblasts. Indeed, fibroblasts projected onto a t-SNE map based on regulon activity reproduced similar upper versus lower dermal fibroblast separation (Figures S6A–S6C), as seen with Seurat clustering (Figure 4H). Intriguingly, we also observed near-complete recapitulation of the highly conserved *Hox* transcriptional program that encodes positional identity and regulates patterning of new HFs in a site-specific fashion within upper dermal fibroblasts (Figure S6B; Rinn et al., 2006, 2008; Yu et al., 2018). This provides compelling evidence that reinstating pre-injury positional identity through reactivation of body plan-specifying TFs may be an important prerequisite for regeneration. We again observed regionalized activation of TFs such as *Fosl2*, *Tcf4*, and *Klf4*, factors that were characterized previously as pan-myofibroblastic markers based on gene expression alone (Figure S6C; Guerrero-Juarez et al., 2019). Among LWC upper dermal fibroblasts, we attempted to identify TFs that may confer an inductive mesenchymal fate to enable WIHN. We found that overlapping activation of TFs forms a continuum, starting from competent *Creb3*^{active} *Foxp1*^{active} LWC upper dermal fibroblasts to *Nfyb*^{active} *Zic1*^{active} *Hey1*^{active} neogenic condensate/DP (Figures S6D–S6F).

Taken together, these data identify several regionally specified fibroblasts states, each enacted by a distinct set of GRN activity that enables competence for WIHN or promotes a scar-forming fate. Surprisingly, it also reveals several highly discrepant GRNs where transcript abundance does not reflect TFs activity for the same factor. This suggests that regionalized fibroblast plasticity maybe driven (at least in part) through post-transcriptional or epigenetic mechanisms, similar to those documented recently during neural lineage transitions (Baser et al., 2019; Stratton et al., 2019).

Epigenetic Signatures Distinguish Fibroblast States within Neogenic Domains

Epigenetic changes accompanying wound healing are poorly understood (Plikus et al., 2015). Two independent observations

hint that epigenomes may serve as key determinants of fibroblast function during regenerative healing. First, we observed robust reactivation of genes and GRNs exclusively expressed in dermal condensate/DP during embryonic HF morphogenesis in non-hair-fated fibroblasts recruited to LWs (Figures 4 and 5A–5C). This implies that interfollicular fibroblasts harbor a latent capacity to undergo significant epigenetic alterations to reactivate early dermal transcriptional states and acquire inductive mesenchymal function. Second, although transcriptional changes may be necessary for skin and HF regeneration, they are not sufficient for key TFs to activate its downstream targets. This raises the possibility that fibroblast epigenetic status may enable or occlude TF activity by modulating genome-wide DNA motif accessibility. To directly test both possibilities, we performed single-cell ATAC-seq to assay genome-wide chromatin accessibility at the LWC 14 dpw (Figure 5D). To first find out whether upper and lower dermal fibroblasts enacted distinct epigenetic landscapes, we compared cells that had *Pdgfra* and *Crabp1* accessible (upper fibroblasts) with those that had *Pdgfra* but not *Crabp1* accessible (lower fibroblasts). This revealed 29,929 peaks, 12,629 promoters, and 579 TF motifs as comparatively enriched features between the two fibroblast populations. Interestingly, comparing accessibility between promoter sums revealed the embryonically active proteoglycan *Lum* (6.6 log₂ fold change) and metabolic regulator *Prr16* (5.8 log₂ fold change) as part of the upper fibroblast chromatin signature (Figure 5E). Among the 579 differentially enriched motifs, we found that a number of TFs were jointly predicted as being differentially accessible and active within upper and lower fibroblasts (Figure 5F). These included homeobox-containing (HOX) B/C family TFs, suggesting that their functional activation maybe a direct consequence of enhanced accessibility of its cognate motifs.

We then wanted to find out whether pairwise correspondence between fibroblasts in the single-cell assay for transposase-accessible chromatin using sequencing (scATAC-seq) and scRNA-seq datasets could reveal HF-associated epigenetic signatures. Because deconvoluting cell states using scATAC-seq measurements alone is difficult because of its sparse binarized structure (S.S., A.T. Ansuman, W. Zhou, H. Ji, J.A.S., A.J., N. Bahlis, S. Morrissy, and J.B., unpublished data), we integrated scATAC-seq with LWC 14 dpw upper dermal fibroblast scRNA-seq (Figures 6D–6F; Stuart et al., 2019). Indeed, we find that emergent HF mesenchymal states are associated with distinct chromatin landscapes to enable precise transcriptional regulation (Figures 6E and 6F). For example, the bone morphogenetic protein (BMP) antagonist *Grem2* is highly accessible over the entire gene body within competent LWC fibroblasts (Figure 6F), but its accessibility is lost following commitment to a HF mesenchymal fate. We also find dynamic changes in distant regulatory elements predicted to be co-accessible with known

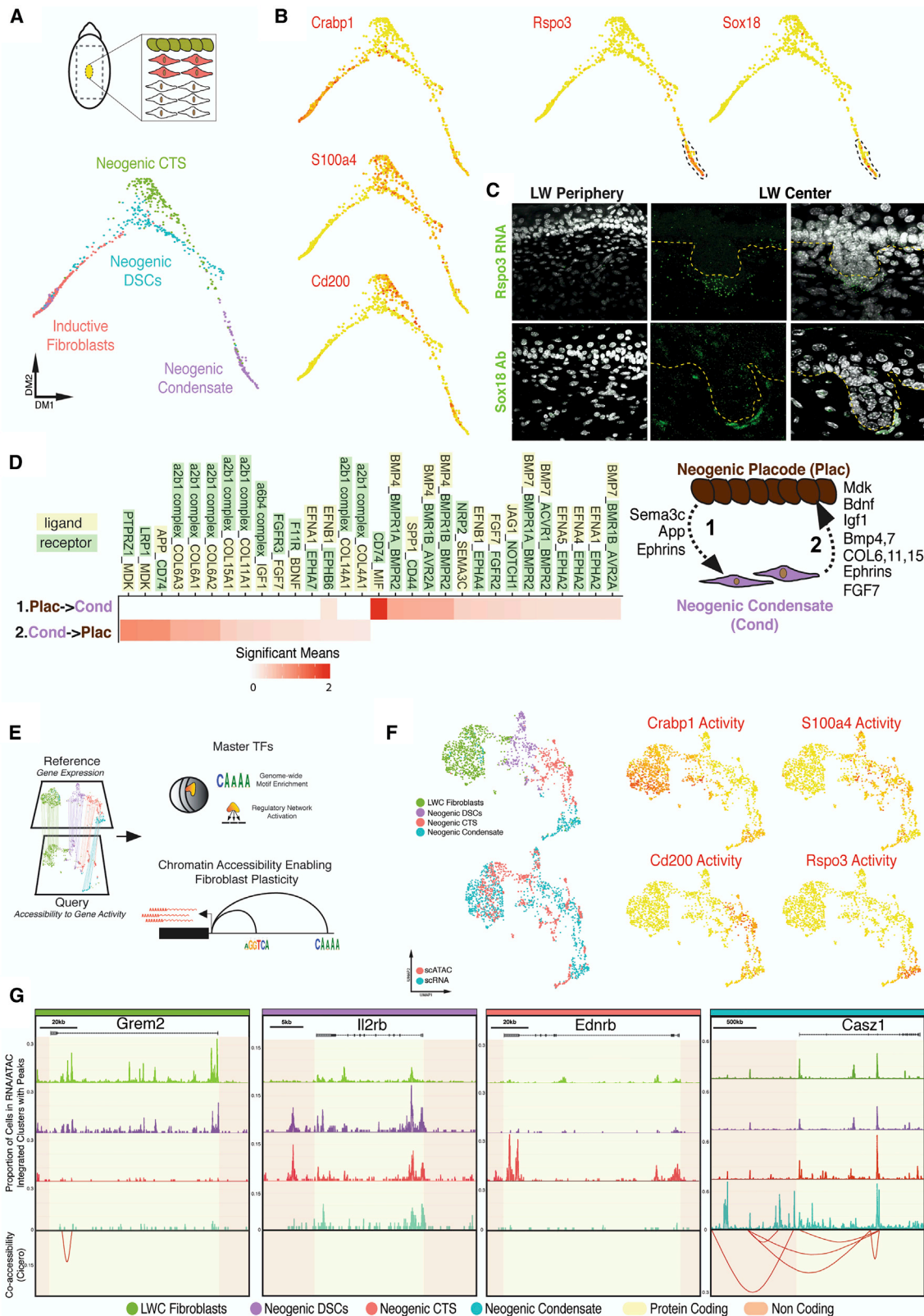
Figure 5. Distinct Regulatory Network Activity Is Enabled by Preferential Chromatin Accessibility to Regeneration-Associated TFs

(A) GRN-based clustering colored by LWC (red) and LWP (blue) fibroblasts reveals distinct regulatory states enacting regionally specified fibroblast responses. (B and C) t-SNE plots showing mRNA (yellow), binary regulon activity (active (blue) or inactive (gray)), and kernel density line AUC histogram plotting TF activation inferred by SCENIC. Examples of differentially active regulons in LWP 14 dpw (B) or LWC 14 dpw (C).

(D) Schematic summarizing scATAC-seq and scRNA-seq measurements from fibroblasts isolated from LWC 14 dpw.

(E) Pseudo-bulk ATAC profiles comparing *Pdgfra*⁺ *Crabp1*⁺ (inductive) versus *Pdgfra*⁺ *Crabp1*⁻ (non-inductive) fibroblasts.

(F) Correspondence between TFs with enrichment in binding motifs (measured by scATAC-seq) and activation of their regulatory networks (GRN inference using scRNA-seq/SCENIC). LWP, LW periphery; AUC, area under the curve; TF, transcription factors.



(legend on next page)

regulators of embryonic skin (as seen with *Cas21*; Figure 6F) and enhanced accessibility paired with concomitant activation of several regulatory TFs, including known HF regulators, such as *Hey1*, within neogenic condensate/DP (Figure S6E). The full list of state-specific peaks, motifs, and pseudo-bulk coverage tracks can be visualized on Wound Atlas (http://www.biernaskielab.ca/wound_atlas; Figure S7D).

Together, our multi-omics characterization unearths complementary layers of regulatory control governing fibroblast function and shortlists key TFs (determined by orthogonal genomic measurements) that may function as important molecular targets for inciting successful dermal regeneration and/or mitigating fibrosis.

Single-Cell Multi-omics Reveal Runx1 and Retinoic Acid as Master Regulators of Mesenchymal Regeneration

To assess the functional significance of regulators identified through multi-omics profiling, we shortlisted retinoic acid (RA) and Runx1 pathways because several TFs driving these networks were exclusively active within regenerative LWC upper dermal fibroblasts (Figures 7A–7D). To determine whether RA and Runx1 signaling were necessary to enable WIHN, we applied small-molecule inhibitors to healing wounds (from 5–18 dpw). Consistent with their putative roles as master regulators of mesenchymal competence, RA and Runx1 inhibition ameliorated the regenerative potential, resulting in 6.3 ± 0.6 and 5.3 ± 0.7 neogenic HFs respectively, compared with 10.1 ± 1.1 HFs in vehicle controls. Conversely, application of exogenous RA augmented the regenerative capacity, resulting in a 1.5-fold increase in neogenic HFs (16.7 ± 1.3 ; Figure 7F; Figure S7A). Together, our data support a highly plastic view of interfollicular fibroblasts recruited to LWs. Not only do they undergo considerable genomic and phenotypic alterations to acquire highly specialized, non-native functions post-injury, but their propensity to do so can be pharmacologically modulated. To enable broad dissemination of identified candidates, we built a searchable companion website called Wound Atlas (http://www.biernaskielab.ca/wound_atlas; Figures S7B–S7D). This platform will be periodically updated as additional data are accrued, with the hope that it will inspire efforts toward modulating mesenchymal dynamics across tissues.

Hic1 Deletion Enhances WIHN by Increasing Fibroblast Density within Regenerative Domains of LWs

Because *Hic1* regulates MP quiescence, and its inactivation results in MP overactivation after skeletal muscle and cardiac damage, leading to fibrosis (Scott et al., 2019; Soliman et al.,

2020), we wanted to find out whether *Hic1* insufficiency would similarly alter dermal wound healing outcomes. To assess the cell-autonomous effect of *Hic1* deletion in isolated dermal progenitors, we FACS-isolated ITG α 8⁺/CD200⁺/tdTomato⁺ dermal progenitors (Shin et al., 2020; Hagner et al., 2020) from α SMA^{CreERT2} Rosa^{tdTomato}; *Hic1*^{fllox/fllox} (or *Hic1*^{fllox/fllox}) and *Hic1*^{WT/WT} mice and grew them *in vitro* in the presence of known mitogens. Consistent with its reported role as a tumor suppressor, we found that *Hic1*^{fllox/fllox} dermal progenitors exhibited a marked increase in colony number relative to littermate *Hic1*^{WT/WT} control cells ($p < 0.05$) (Figures S7B–S7C). Remarkably, the effect of *Hic1* deficiency on proliferation was further magnified (nearly a 5-fold increase) when secondary colony formation was examined (Figure S7C). Next we wanted to find out whether *Hic1* deletion within wound-activated α SMA⁺ myofibroblasts (using the same α SMA^{CreERT2} Rosa^{tdTomato}; *Hic1*^{fllox/fllox} mice) altered WIHN. Intriguingly, although *Hic1* inactivation at early wound stages (2–6 dpw; Figure 7G) resulted in a dramatic 4-fold increase in the number of neogenic HFs (*Hic1*^{WT/WT}, 7.3 ± 2.1 HFs; *Hic1*^{fllox/fllox}, 29.7 ± 9.3 HFs; Figures 7G–7I), late-stage inactivation (12–16 dpw) had no effect on WIHN (Figures 7K–7M). This enhanced regenerative capacity was associated with a significantly higher α SMA-tdTomato⁺ fibroblast density specifically within the central regenerative domain but not in the peripheral scar-forming domain of LWs (Figure 7N). Together, this supports the notion that *Hic1* deficiency does not intrinsically bias fibroblasts to adopt a pro-fibrotic response but, rather, that fibroblasts are equally amenable to adopt regenerative competence when exposed to an appropriately permissive environment. Transient modulation of *Hic1* to more effectively mobilize skin MPs during wound healing, coupled with provision of a permissive (pro-regenerative) wound environment, may represent a viable therapeutic approach to enhance wound healing outcomes.

DISCUSSION

Despite their innate regenerative propensity, self-renewing hfDSCs and their progeny made only modest contributions to wound repair and HF neogenesis. Rather, extrafollicular fibroblast pools derived from *Hic1*-expressing MPs were the primary source of reparative fibroblasts in adult mouse skin. These findings contradict the notion that migration and reassembly of pre-existing, “pro-regenerative” HF progenitors are necessary for skin regeneration. Rather, our data support the view that, when provided with a permissive environment, such as that found in the LWC, mobilized interfollicular fibroblasts are able to acquire regenerative competence and make robust contributions to *de*

Figure 6. Epigenetic Changes in Chromatin Accessibility Underlie Fibroblast Functional Divergence within Regenerative Domains of LWs (A and B) DM of LWC upper dermal fibroblasts reveals continuity of transcriptional states (A) connecting inductive *Crabp1*⁺ upper dermal fibroblasts to *Crabp1*⁺ *Rspo3*⁺ *Sox18*⁺ neogenic condensate (B).

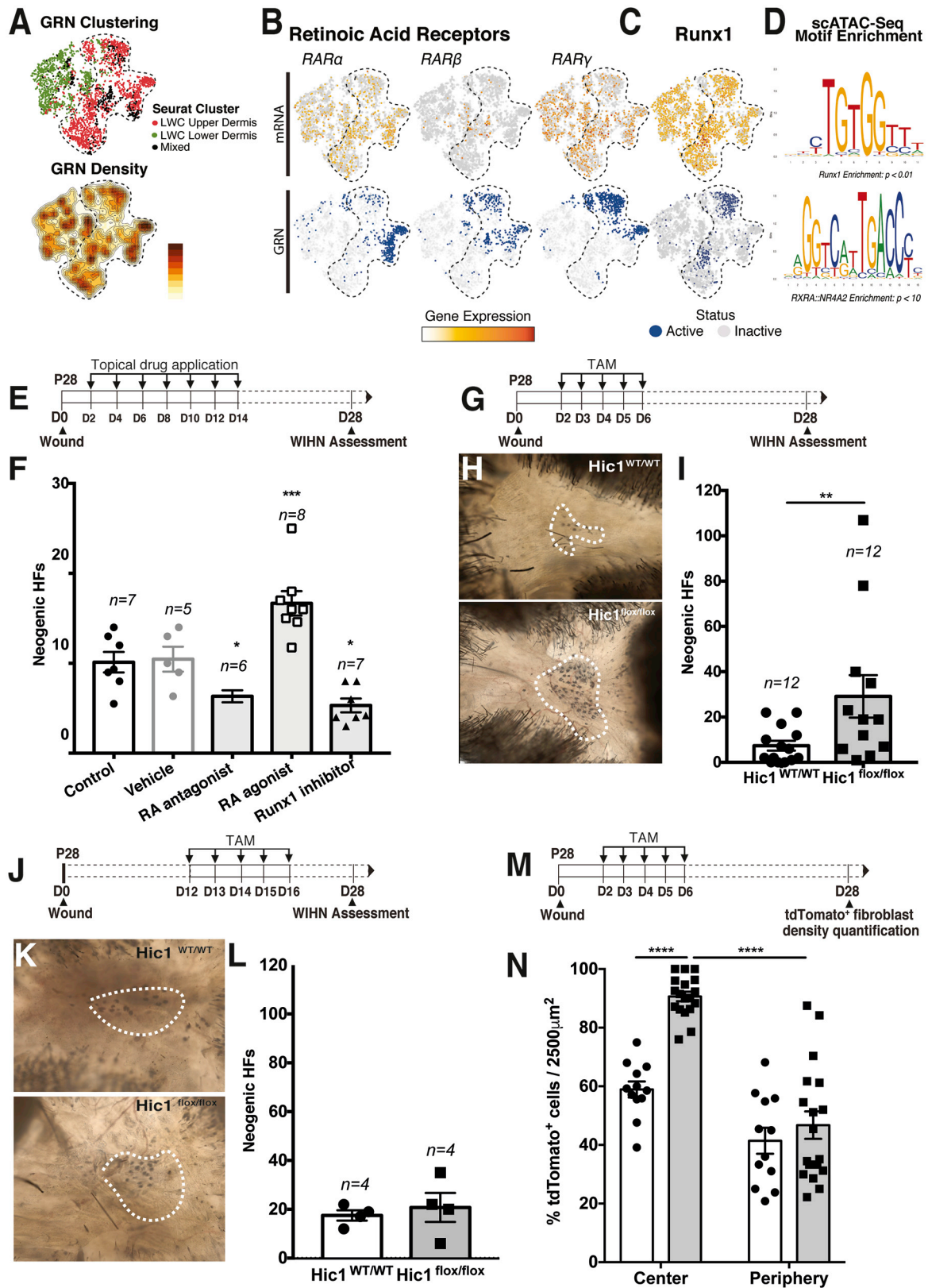
(C) *Rspo3* RNA and Sox18 protein in neogenic condensate cells within the LWC.

(D) Epithelial (brown)-mesenchymal (purple) crosstalk between *Rspo3*⁺ *Sox18*⁺ neogenic condensate-epithelial placode reveals a striking resemblance to signals during HF morphogenesis. Ligands are highlighted in yellow. Receptors are highlighted in green.

(E) Schematic summarizing integrated transcriptomic (scRNA-seq) and epigenomic (scATAC-seq) assessment of regeneration-competent LWC fibroblasts.

(F) Uniform Manifold Approximation and Projection (UMAP) of *Crabp1*⁺ inductive fibroblasts queried for features marking HF mesenchymal fates.

(G) Pseudo-bulk ATAC profiles of integrated fibroblast states show enriched accessibility near embryonic fibroblast (i.e., *Grem2* and *Cas21*) and HF marker (i.e., *Ednrb*) genes. DSC, dermal stem cell; CTS, connective tissue sheath.



(legend on next page)

novo HF morphogenesis and adipogenesis following injury. Thus, wound-activated fibroblasts, irrespective of their origins within uninjured skin, harbor a latent regenerative capacity that can be unmasked when exposed to a permissive environment. Our observations mirror the epithelial origin of neogenic HFs because progeny of pre-existing HF epithelial stem/progenitors do not contribute to WIHN (Ito et al., 2007). These converging lines of evidence emphasize the cellular plasticity (epithelial and mesenchymal) that is unmasked given exposure to appropriate microenvironmental cues.

Single-cell profiling of fibroblasts within central domains of LWs revealed significant transcriptional, regulatory, and epigenetic divergence from the fibrotic periphery of LW or SW fibroblasts that enables acquisition of a regenerative state. Intriguingly, several TFs predicted to drive the observed gene expression patterns also exhibited an over-representation of sequence motifs in our scATAC-seq measurements. For example, a unique combination of *Hox* TFs (i.e., *c6*, *c8*, and *a10*) that maintain HF and dorsal dermal spatial identity in adult skin (Yu et al., 2018) were reactivated (and several corresponding TF motifs that showed enhanced accessibility) specifically within regeneration-competent fibroblasts. Hence, regionalized re-establishment of mesenchymal positional identity may be a necessary step in acquiring regenerative competence.

The ligand-inducible retinoic acid receptor (RAR) and Runx1 TFs were also jointly predicted by single-cell multi-omics as drivers of mesenchymal competence. RA synthesis, triggered by damage-induced double-stranded RNA (dsRNA) release, acts to prime epidermal keratinocytes for WIHN through TLR3 activation (Kim et al., 2019). Here we propose that RA also simultaneously unmasks mesenchymal competence for regeneration by activating its nuclear receptors (RARs), which drives a distinct downstream regulatory network (including several dermal condensate genes such as *Enpp2*, *Hck*, and *Heyl*) in a regionalized fashion. Similarly, activation of Runx1, a TF that, in turn, activates *Stat3* (Scheitz et al., 2012), also a key initiator of WIHN (Nelson et al., 2015), has been shown to promote mesenchymal proliferation, whereas its deficiency is linked to actin polymerization and myofibroblast differentiation (Kim et al., 2014). Indeed, our *in vivo* pharmacologic studies confirm that RARs and Runx1 are key mesenchymal regulators of regenerative competence and that perturbations of these networks would affect healing.

Given that interfollicular *Hic1*-lineage cells bear a striking resemblance to MPs in skeletal muscle and the heart, we wanted to find out whether a common set of lineage programs regulates their response to insult and possibly unmasks their pathogenic potential. An obvious candidate was the transcriptional repressor *Hic1*, considering that its inactivation within

cardiac and skeletal muscle MPs leads to a hyperactivated MP response that drives excessive fibrotic scarring (Scott et al., 2019; Kim and Braun, 2020; Soliman et al., 2020). Intriguingly, although *Hic1* inactivation predictably increased proliferation in isolated and wound-activated dermal progenitors, it paradoxically enhanced regeneration following skin injury, as indicated by a marked increase in neogenic HFs. Although consistent with the broader notion that *Hic1* inactivation licenses fibroblast activation across different tissues, our results highlight how different environmental contexts shape their final fate and function. Although notexin-induced skeletal muscle damage triggers ectopic fibroblast expansion followed by rapid clearance (leaving behind only a small pool of quiescent MPs that reoccupy their perivascular niche), a sustained fibroblast presence in neodermis is crucial for restoring dermal architecture. Thus, recruiting additional fibroblasts within the central pro-regenerative microenvironment of large skin wounds enhances tissue neomorphogenesis, whereas excess MP derivatives in skeletal muscle and the heart contribute to persistent fibrofatty deposits and pathogenic repair. Our dissection of regulatory programs casts new light on how functional diversity among fibroblasts is enacted post-wounding. Our companion website, Wound Atlas, will enable further exploration of the molecular regulators of mesenchymal fate and function. Because *Hic1*-lineage MPs appear to share overlapping regulatory mechanisms, modulation of identified networks may be useful in mitigating fibrosis and promoting mesenchymal regeneration across various organ systems (Scott et al., 2019; Soliman et al., 2020).

In summary, when provided with a permissive environment, mobilized extrafollicular fibroblasts that originate from *Hic1*-expressing MPs are able to acquire inductive mesenchymal fates that subsequently participate in HF neogenesis. Assumption of regenerative competence in mobilized fibroblasts occurs by reactivating distinct, embryonic-like regulatory states upon entry into pro-regenerative (central) wound microenvironments. Together, these findings clarify cellular and molecular targets for future interventions designed to exploit this latent regenerative capacity and, ultimately, improve wound healing outcomes.

Limitations of Study

Pooling of wound tissues from sex-controlled biological replicates for single-cell genomic experiments precluded unbiased assessment of biologic or sex-specific variations contributing to fibroblast states. Although single-cell ATAC-seq measurements from LWC cells compare regeneration-competent versus non-regenerative fibroblasts, it precludes determination of differential chromatin/motif accessibility between fibroblasts

Figure 7. Perturbing Regulators of Mesenchymal Regenerative Competence Alters Skin Regeneration

(A–C) GRN-based clustering colored by LWC upper and lower dermal fibroblasts (A) revealed RARs (B) and Runx1 (C). (D) Pseudo-bulk ATAC-seq profiles of Runx1 and RXRA::NR4A2 heterodimer binding motifs overrepresented in *Crabp1*⁺ inductive fibroblasts. (E and F) Pharmacologic modulation of RAR and Runx1 during wound healing (E) alters HF neogenesis (F). (G) Experimental design of early TAM-inducible *Hic1* deletion within α SMA:tdTomato⁺ fibroblasts. (H and I) Representative pictures (H) and quantification of neogenic HFs (I) following *Hic1* deletion. (J) Experimental design of late TAM-inducible *Hic1* deletion within α SMA:tdTomato⁺ fibroblasts. (K and L) Representative pictures (K) and quantification of neogenic HFs (L) following late *Hic1* deletion. (M) Protocol (M) and α SMA:tdTomato⁺ fibroblast density quantification (N) within different wound domains at P28 (n = 12). Data are mean \pm SEM. *p < 0.05, **p < 0.005, ***p < 0.0005, ****p < 0.0001. LWC, large wound center; HF, hair follicle; TAM, tamoxifen; RAR, retinoic acid receptor.

recruited to different wound regions (LWC versus LWP) or wound type (SWs versus LWs).

STAR★METHODS

Detailed methods are provided in the online version of this paper and include the following:

- KEY RESOURCES TABLE
- RESOURCE AVAILABILITY
 - Lead Contact
 - Materials Availability
 - Data and Code Availability
- EXPERIMENTAL MODEL AND SUBJECT DETAILS
 - Mice
- METHOD DETAILS
 - Wound-Induced Hair follicle Neogenesis (WIHN) assay
 - Histology, immunofluorescence staining and image analysis
 - Cell isolation and ex-vivo HF formation assay
 - Single-cell RNA-Seq library construction
 - Gene Regulatory Network analysis
 - Single-cell ATAC-Seq
 - Fluorescence *In Situ* Hybridization (RNAScope)
 - Topical application of candidate compounds
 - Conditional deletion of *Hic1*
- QUANTIFICATION AND STATISTICAL ANALYSIS
- ADDITIONAL RESOURCES
 - Wound Atlas

SUPPLEMENTAL INFORMATION

Supplemental Information can be found online at <https://doi.org/10.1016/j.stem.2020.07.008>.

ACKNOWLEDGMENTS

This work was supported by the Canadian Institutes of Health Research (MOP-106646 and PJT-401394 to J.B., PJT-148816 to T.M.U., and FDN-159908 to F.M.R.) and the Calgary Firefighters Burn Treatment Society. S.A. was supported by a UCVM Dean's Excellence Award. S.S. was supported by CIHR Vanier, Alberta Innovates (AI), and Killam doctoral scholarships. E.L. and J.A.S. were supported by Alberta Children's Hospital Research Institute postdoctoral fellowships. W.R. was supported by an AI MD/PhD scholarship. N.L.R. was a UCalgary Eyes High postdoctoral scholar. N.S. was supported by a CIHR master's scholarship. We thank M. Workentine (informatics), M. Cheng (reagent ordering), and M. Hurtatis, M. Chisholm, and R. Villanueva Gamutin (animal care). The graphical abstract was created with BioRender.

AUTHOR CONTRIBUTIONS

S.A. performed *Hic1* lineage tracing in uninjured skin, in WIHN setting, and animal experiments for scRNA-seq. S.S. performed scRNA-seq, scATAC-seq, and bioinformatics analyses. E.L. performed *in vivo* drug screens and contributed to scRNA-seq and scATAC-seq. E.L., G.Y., and A.H. performed *Hic1* deletion experiments. P.S., A.H., E.L., A.J., R.A., and J.A.S. contributed to scRNA-seq experiments and analyses. A.J., R.A., and S.S. developed Wound Atlas. W.R. performed *Hic1* lineage tracing in uninjured adult skin with S.S. N.L.R. performed flow cytometry. N.S. performed *in situ* hybridizations. J.Y. and A.I. performed FACS. A.U. helped for *Hic1*:tdTomato colony maintenance. W.S. and T.M.U. generated *Hic1*^{CreERT2}:tdTomato mice. C.-K.C. and F.M.V.R. performed parabiosis experiments. J.B. conceived the experiments, supervised the study, and co-wrote the manuscript with S.S., S.A., and E.L. All authors approved the final version of the manuscript.

DECLARATION OF INTERESTS

The authors declare no competing interests.

Received: March 25, 2020

Revised: May 25, 2020

Accepted: July 9, 2020

Published: August 4, 2020

REFERENCES

- Aibar, S., González-Blas, C.B., Moerman, T., Huynh-Thu, V.A., Imrichova, H., Hulselmans, G., Rambow, F., Marine, J.C., Geurts, P., Aerts, J., et al. (2017). SCENIC: single-cell regulatory network inference and clustering. *Nat. Methods* **14**, 1083–1086.
- Baser, A., Skabkin, M., Kleber, S., Dang, Y., Gülcüler Baltas, G.S., Kalamakis, G., Göpferich, M., Ibañez, D.C., Schefzik, R., Lopez, A.S., et al. (2019). Onset of differentiation is post-transcriptionally controlled in adult neural stem cells. *Nature* **566**, 100–104.
- Biernaskie, J., Paris, M., Morozova, O., Fagan, B.M., Marra, M., Pevny, L., and Miller, F.D. (2009). SKPs derive from hair follicle precursors and exhibit properties of adult dermal stem cells. *Cell Stem Cell* **5**, 610–623.
- Budnick, I., Hamburg-Shields, E., Chen, D., Torre, E., Jarrell, A., Akhtar-Zaidi, B., Cordovan, O., Spitale, R.C., Scacheri, P., and Atit, R.P. (2016). Defining the identity of mouse embryonic dermal fibroblasts. *Genesis* **54**, 415–430.
- Cadau, S., Rosignoli, C., Rhetore, S., Voegel, J., Parenteau-Bareil, R., and Berthod, F. (2013). Early stages of hair follicle development: a step by step microarray identity. *Eur. J. Dermatol.* Published online April 8, 2013. <https://doi.org/10.1684/ejd.2013.1972>.
- Driskell, R.R., Lichtenberger, B.M., Hoste, E., Kretschmar, K., Simons, B.D., Charalambous, M., Ferron, S.R., Herault, Y., Pavlovic, G., Ferguson-Smith, A.C., and Watt, F.M. (2013). Distinct fibroblast lineages determine dermal architecture in skin development and repair. *Nature* **504**, 277–281.
- Eming, S.A., Martin, P., and Tomic-Canic, M. (2014). Wound repair and regeneration: mechanisms, signaling, and translation. *Sci. Transl. Med.* **6**, 265sr6.
- Fan, C., Luedtke, M.A., Prouty, S.M., Burrows, M., Kollias, N., and Cotsarelis, G. (2011). Characterization and quantification of wound-induced hair follicle neogenesis using *in vivo* confocal scanning laser microscopy. *Skin Res. Technol.* **17**, 387–397.
- Genander, M., Holmberg, J., and Frisén, J. (2010). Ephrins negatively regulate cell proliferation in the epidermis and hair follicle. *Stem Cells* **28**, 1196–1205.
- González, R., Moffatt, G., Hagner, A., Sinha, S., Shin, W., Rahmani, W., Chojnacki, A., and Biernaskie, J. (2017). Platelet-derived growth factor signaling modulates adult hair follicle dermal stem cell maintenance and self-renewal. *NPJ Regen. Med.* **2**, 11.
- Guerrero-Juarez, C.F., Dedhia, P.H., Jin, S., Ruiz-Vega, R., Ma, D., Liu, Y., Yamaga, K., Shestova, O., Gay, D.L., Yang, Z., et al. (2019). Single-cell analysis reveals fibroblast heterogeneity and myeloid-derived adipocyte progenitors in murine skin wounds. *Nat. Commun.* **10**, 650.
- Haghverdi, L., Büttner, M., Wolf, F.A., Buettner, F., and Theis, F.J. (2016). Diffusion pseudotime robustly reconstructs lineage branching. *Nat. Methods* **13**, 845–848.
- Hagner, A., Shin, W., Sinha, S., Alpaugh, W., Workentine, M., Abbasi, S., Rahmani, W., Agabalyan, N., Sharma, N., Sparks, H., et al. (2020). Transcriptional profiling of the adult hair follicle mesenchyme reveals R-spondin as a novel regulator of dermal progenitor function. *iScience* **23**, 101019.
- Ito, M., Yang, Z., Andl, T., Cui, C., Kim, N., Millar, S.E., and Cotsarelis, G. (2007). Wnt-dependent *de novo* hair follicle regeneration in adult mouse skin after wounding. *Nature* **447**, 316–320.
- Jahoda, C.A.B., and Reynolds, A.J. (2001). Hair follicle dermal sheath cells: unsung participants in wound healing. *Lancet* **358**, 1445–1448.
- Joost, S., Annusver, K., Jacob, T., Sun, X., Dalessandri, T., Sivan, U., Sequeira, I., Sandberg, R., and Kasper, M. (2020). The molecular anatomy of mouse skin during hair growth and rest. *Cell Stem Cell* **26**, 441–457.e7.

- Kim, J., and Braun, T. (2020). Keeping Fibrotic Responses in Contractile Tissues at Bay: The Plot t(Hic1)ens. *Cell Stem Cell* 26, 129–130.
- Kim, W., Barron, D.A., San Martin, R., Chan, K.S., Tran, L.L., Yang, F., Ressler, S.J., and Rowley, D.R. (2014). RUNX1 is essential for mesenchymal stem cell proliferation and myofibroblast differentiation. *Proc. Natl. Acad. Sci. U.S.A.* 111, 16389–16394.
- Kim, D., Chen, R., Sheu, M., Kim, N., Kim, S., Islam, N., Wier, E.M., Wang, G., Li, A., Park, A., et al. (2019). Noncoding dsRNA induces retinoic acid synthesis to stimulate hair follicle regeneration via TLR3. *Nat. Commun.* 10, 2811.
- Lim, C.H., Sun, Q., Ratti, K., Lee, S.H., Zheng, Y., Takeo, M., Lee, W., Rabbani, P., Plikus, M.V., Cain, J.E., et al. (2018). Hedgehog stimulates hair follicle neogenesis by creating inductive dermis during murine skin wound healing. *Nat. Commun.* 9, 4903.
- Muramatsu, T. (1993). Midkine (MK), the product of a retinoic acid responsive gene, and pleiotrophin constitute a new protein family regulating growth and differentiation. *Int. J. Dev. Biol.* 37, 183–188.
- Nelson, A.M., Reddy, S.K., Ratliff, T.S., Hossain, M.Z., Katseff, A.S., Zhu, A.S., Chang, E., Resnik, S.R., Page, C., Kim, D., et al. (2015). dsRNA Released by Tissue Damage Activates TLR3 to Drive Skin Regeneration. *Cell Stem Cell* 17, 139–151.
- Pennisi, D., Bowles, J., Nagy, A., Muscat, G., and Koopman, P. (2000). Mice null for *sox18* are viable and display a mild coat defect. *Mol. Cell Biol.* 20, 9331–9336.
- Plikus, M.V., Guerrero-Juarez, C.F., Ito, M., Rose Li, Y., Dedhia, P.H., Zheng, Y., Shao, M., Gay, D.L., Ramos, R., Hsi, T.C., et al. (2017). Regeneration of fat cells from myofibroblasts during wound healing. *Science* 355 (6326), 748–752, <https://doi.org/10.1126/science.aai8792>.
- Plikus, M.V., Guerrero-Juarez, C.F., Treffeisen, E., and Gay, D.L. (2015). Epigenetic control of skin and hair regeneration after wounding. *Exp. Dermatol.* 24, 167–170.
- Pliner, H.A., Packer, J.S., McFaline-Figueroa, J.L., Cusanovich, D.A., Daza, R.M., Aghamirzaie, D., Srivatsan, S., Qiu, X., Jackson, D., Minkina, A., et al. (2018). Cicero Predicts cis-Regulatory DNA Interactions from Single-Cell Chromatin Accessibility Data. *Mol. Cell* 71, 858–871.e8.
- Rahmani, W., Abbasi, S., Hagner, A., Raharjo, E., Kumar, R., Hotta, A., Magness, S., Metzger, D., and Biernaskie, J. (2014). Hair follicle dermal stem cells regenerate the dermal sheath, repopulate the dermal papilla, and modulate hair type. *Dev. Cell* 31, 543–558.
- Rendl, M., Lewis, L., and Fuchs, E. (2005). Molecular dissection of mesenchymal-epithelial interactions in the hair follicle. *PLoS Biol.* 3, e331.
- Rinkevich, Y., Walmsley, G.G., Hu, M.S., Maan, Z.N., Newman, A.M., Drukker, M., Janusz, M., Krampitz, G.W., Gurtner, G.C., Lorenz, H.P., et al. (2015). Skin fibrosis. Identification and isolation of a dermal lineage with intrinsic fibrogenic potential. *Science* 348, aaa2151.
- Rinn, J.L., Bondre, C., Gladstone, H.B., Brown, P.O., and Chang, H.Y. (2006). Anatomic demarcation by positional variation in fibroblast gene expression programs. *PLoS Genet.* 2, e119.
- Rinn, J.L., Wang, J.K., Allen, N., Brugmann, S.A., Mikels, A.J., Liu, H., Ridky, T.W., Stadler, H.S., Nusse, R., Helms, J.A., and Chang, H.Y. (2008). A dermal HOX transcriptional program regulates site-specific epidermal fate. *Genes Dev.* 22, 303–307.
- Rivera-Gonzalez, G.C., Shook, B.A., Andrae, J., Holtrup, B., Bollag, K., Betsholtz, C., Rodeheffer, M.S., and Horsley, V. (2016). Skin adipocyte stem cell self-renewal is regulated by a PDGFA/AKT-signaling axis. *Cell Stem Cell* 19, 738–751.
- Satija, R., Farrell, J.A., Gennert, D., Schier, A.F., and Regev, A. (2015). Spatial reconstruction of single-cell gene expression data. *Nat. Biotechnol.* 33, 495–502.
- Scheitz, C.J.F., Lee, T.S., McDermitt, D.J., and Tumber, T. (2012). Defining a tissue stem cell-driven Runx1/Stat3 signalling axis in epithelial cancer. *EMBO J.* 31, 4124–4139.
- Scott, R.W., Arostegui, M., Schweitzer, R., Rossi, F.M.V., and Underhill, T.M. (2019). Hic1 Defines Quiescent Mesenchymal Progenitor Subpopulations with Distinct Functions and Fates in Skeletal Muscle Regeneration. *Cell Stem Cell* 25, 797–813.e9.
- Seifert, A.W., Kiama, S.G., Seifert, M.G., Goheen, J.R., Palmer, T.M., and Maden, M. (2012). Skin shedding and tissue regeneration in African spiny mice (*Acomys*). *Nature* 489, 561–565.
- Sennett, R., Wang, Z., Rezza, A., Grisanti, L., Roitershtein, N., Sicchio, C., Mok, K.W., Heitman, N.J., Clavel, C., Ma'ayan, A., and Rendl, M. (2015). An integrated transcriptome atlas of embryonic hair follicle progenitors, their niche, and the developing skin. *Dev. Cell* 34, 577–591.
- Shin, W., Rosin, N.L., Sparks, H., Sinha, S., Rahmani, W., Sharma, N., Workentine, M., Abbasi, S., Labit, E., Stratton, J.A., and Biernaskie, J. (2020). Dysfunction of hair follicle mesenchymal progenitors contributes to age-associated hair loss. *Dev. Cell* 53, 185–198.e7.
- Shook, B.A., Wasko, R.R., Rivera-Gonzalez, G.C., Salazar-Gatzimas, E., López-Giráldez, F., Dash, B.C., Muñoz-Rojas, A.R., Aultman, K.D., Zwick, R.K., Lei, V., et al. (2018). Myofibroblast proliferation and heterogeneity are supported by macrophages during skin repair. *Science* 362, eaar2971.
- Silva-Vargas, V., Celso, C.L., Giangreco, A., Ofstad, T., Prowse, D.M., Braun, K.M., and Watt, F.M. (2005). β -Catenin and Hedgehog signal strength can specify number and location of hair follicles in adult epidermis without recruitment of bulge stem cells. *Dev. Cell* 9, 121–131.
- Soliman, H., Paylor, B., Wilder Scott, R., Lemos, D.R., Chang, C., Arostegui, M., Low, M., Lee, C., Fiore, D., Braghetta, P., et al. (2020). Pathogenic potential of Hic1-expressing cardiac stromal progenitors. *Cell Stem Cell* 26, 205–220.e8.
- Stratton, J.A., Shah, P., Sinha, S., Crowther, E., and Biernaskie, J. (2019). A tale of two cousins: Ependymal cells, quiescent neural stem cells and potential mechanisms driving their functional divergence. *FEBS J.* 286, 3110–3116.
- Stratton, J.A., Sinha, S., Shin, W., Labit, E., Chu, T.H., Shah, P.T., Midha, R., and Biernaskie, J. (2019b). Droplet Barcoding-Based Single Cell Transcriptomics of Adult Mammalian Tissues. *J. Vis. Exp.* Published online January 10, 2019. <https://doi.org/10.3791/58709>.
- Stuart, T., Butler, A., Hoffman, P., Hafemeister, C., Papalexi, E., Mauck, W.M., 3rd, Hao, Y., Stoeckius, M., Smibert, P., and Satija, R. (2019). Comprehensive Integration of Single-Cell Data. *Cell* 177, 1888–1902.e21.
- Vento-Tormo, R., Efremova, M., Botting, R.A., Turco, M.Y., Vento-Tormo, M., Meyer, K.B., Park, J.E., Stephenson, E., Polański, K., Goncalves, A., et al. (2018). Single-cell reconstruction of the early maternal-fetal interface in humans. *Nature* 563, 347–353.
- Wang, X., Hsi, T.C., Guerrero-Juarez, C.F., Pham, K., Cho, K., McCusker, C.D., Monuki, E.S., Cho, K.W., Gay, D.L., and Plikus, M.V. (2015). Principles and mechanisms of regeneration in the mouse model for wound-induced hair follicle neogenesis. *Regeneration (Oxf.)* 2, 169–181.
- Wang, X., Chen, H., Tian, R., Zhang, Y., Drutskaya, M.S., Wang, C., Ge, J., Fan, Z., Kong, D., Wang, X., et al. (2017). Macrophages induce AKT/ β -catenin-dependent Lgr5⁺ stem cell activation and hair follicle regeneration through TNF. *Nat. Commun.* 8, 14091.
- Yu, Z., Jiang, K., Xu, Z., Huang, H., Qian, N., Lu, Z., Chen, D., Di, R., Yuan, T., Du, Z., et al. (2018). Hoxc-dependent mesenchymal niche heterogeneity drives regional hair follicle regeneration. *Cell Stem Cell* 23, 487–500.
- Zappia, L., and Oshlack, A. (2018). Clustering trees: a visualization for evaluating clusterings at multiple resolutions. *GigaScience* 7, gjy083.
- Zheng, Y., Du, X., Wang, W., Boucher, M., Parimoo, S., and Stenn, K. (2005). Organogenesis from dissociated cells: generation of mature cycling hair follicles from skin-derived cells. *J. Invest. Dermatol.* 124, 867–876.
- Zheng, G.X.Y., Terry, J.M., Belgrader, P., Ryvkin, P., Bent, Z.W., Wilson, R., Ziraldo, S.B., Wheeler, T.D., McDermott, G.P., Zhu, J., et al. (2017). Massively parallel digital transcriptional profiling of single cells. *Nat. Commun.* 8, 14049.

STAR★METHODS

KEY RESOURCES TABLE

REAGENT or RESOURCE	SOURCE	IDENTIFIER
Antibodies		
Rabbit anti-Keratin5	Biolegend	Cat# 905504; RRID: AB_2616956
Rabbit anti-Keratin14	Biolegend	Cat# 905304; RRID: AB_2616896
Goat anti-ITGa8	R&D Systems	Cat# AF4076; RRID: AB_2296280
Goat anti-ITGa9	R&D Systems	Cat# AF3824; RRID: AB_1151977
Rat anti-CD200	Abcam	Cat# ab33734; RRID: AB_726239
Anti-CD133-AF 488	Sigma-Aldrich	Cat# 53-1331-80; RRID: AB_529615
Chicken anti-GFP	Millipore	Cat# AB3080; RRID: AB_91337
Rabbit anti-Versican	Millipore	Cat# AB0133
Goat anti-Sox18	Santa Cruz BT	Cat# sc-166025; RRID: AB_2195662
Goat anti-P-Cadherin	R&D Systems	Cat# AF761; RRID: AB_355581
Rat anti-Ki67	Dako	Cat# M7249; RRID: AB_2250503
Rabbit anti-Lef1	Cell Signaling	Cat# 2230; RRID: AB_823558
Goat anti-CD26	R&D Systems	Cat# AF954; RRID: AB_355739
Rat anti-CD31	Acris antibodies	Cat# BM4086; RRID: AB_975771
Rabbit anti-FABP4	R&D Systems	Cat# AF1443; RRID: AB_2102444
Goat anti-Rabbit Alexa Fluor 488/555/647	Life Technologies	N/A
Goat anti-Rat Alexa Fluor 488/555/647	Life Technologies	N/A
Donkey anti-Goat Alex Fluor 488/555/647	Life Technologies	N/A
Chemicals, Peptides, and Recombinant Proteins		
Tamoxifen (Z-4-Hydroxy-tamoxifen)	Sigma-Aldrich	H-7904
Metacam	Boehringer Ingelheim	NADA 141-219
Paraformaldehyde (PFA)	Sigma-Aldrich	441244
Clear Frozen Section Compound	VWR	95057-838
RNAscope Fluorescent Multiplex Reagent Kit	Advanced Cell Diagnostics	320850
Hoechst 33258	Sigma-Aldrich	14530
Normal Goat Serum	Jackson ImmunoResearch	005-000-121
Collagenase IV	Sigma-Aldrich	C5138
Dispase 5	StemCell Technologies	7913
HBSS	GIBCO	14175-095
Fluorescence Mounting Media, Mounting Media	Agilent	S303380-2
Trypsin	Sigma-Aldrich	441244
Fetal Bovine Serum (FBS)	Thermo Fisher	SH30071.02
DMEM	ThermoFisher	11885076
Bovine Albumin Serum(BSA) Solution	Sigma-Aldrich	19576
Runx1 inhibitor	Tocris Bioscience	Ro 5-3335
All-trans Retinoic Acid agonist	Tocris Bioscience	0695
Retinoic Acid Antagonist BMS 493	Sigma-Aldrich	B6688
DMSO Gel	Medivet	N/A
Critical Commercial Assays		
BD Facs Aria III	BD Biosciences	N/A
RNAscope 2.0 HD Detection Kit	ACDBio	N/A
10X Chromium Controller	10X Genomics	N/A

(Continued on next page)

Continued

REAGENT or RESOURCE	SOURCE	IDENTIFIER
Chromium Single Cell A Chip kit, 48 rxns	10X Genomics	120236
Chromium Single cell 3' Library & Gel beaded kit V2, 16 rxns	10X Genomics	120237
Chromium i7 multiplex Kit 96 rxns	10X Genomics	120262
Chromium Chip E Single Cell ATAC kit	10X Genomics	1000086
Chromium Single Cell ATAC library & Gel Bead Kit	10X Genomics	1000111
Chromium i7 multiplex Kit N, Set A 96 rxns	10X Genomics	1000084
Illumina HiSeq 4000	Illumina, Genome Quebec	N/A
Deposited Data		
Gene Expression Omnibus (GEO) sc-RNA-seq	This paper	GEO: GSE108677
Gene Expression Omnibus (GEO) sc-ATAC-seq	This paper	GEO: GSE131600
Gene Expression Omnibus (GEO) sc-RNA-seq Muscle MP	Scott et al., 2019	GEO: GSM2976778
Gene Expression Omnibus (GEO) sc-RNA-seq Heart MP	Soliman et al., 2020	GEO: GSM2976778
Experimental Models: Organisms/Strains		
aSMA ^{creERT2} ; Rosa ^{YFP}	Rahmani et al., 2014	N/A
Hic1 ^{creERT2} ; Rosa ^{tdTomato}	Scott et al., 2019	N/A
Nu/Nu	Charles River	N/A
aSMA ^{creERT2} tdTomato ⁺ ; Hic1 ^{flox/flox}	This paper	N/A
C57BL/6J	Charles River	N/A
Oligonucleotides		
YFP	UofC Core DNA services	N/A
Cre	UofC Core DNA services	N/A
tdTomato	UofC Core DNA services	N/A
Hic1 flox	UofC Core DNA services	N/A
Software and Algorithms		
R	R	3.4, 3.5, 3.6
RStudio	RStudio	1.2.5042
Cellranger	10X Genomics	3.1.0
Seurat	Satija Lab	v.2.3, 3.0, 3.1
SCENIC	Aerts Lab	1.0.0.3
RcisTarget	Aerts Lab	v.1.2.1
AUCell	Aerts Lab	v.1.4.1
Cicero	Trapnell Lab	v.1.3.1
Illustrator CC	Adobe	CC 2015
Photoshop CC	Adobe	CC 2015
ggplot2	Tidyverse	v.3.1.1
Prism 6	GraphPad	6.01
Prism 7	GraphPad	7.01
Microsoft Excel	Microsoft	2016
CellPhoneDB	CellPhoneDB.org	v.1
clustree	Oshlack Lab	v. 0.4.2
R Shiny	https://shiny.rstudio.com/	v.1.4.0.2
shinythemes	CRAN	v.1.1.2
shinyLP	CRAN	v.1.1.2
Cellranger-ATAC	10X Genomics	v.1.1.0

(Continued on next page)

Continued

REAGENT or RESOURCE	SOURCE	IDENTIFIER
Loupe Browser	10X Genomics	3.1.0
BioRender	BioRender.com	N/A
Leica software	Leica	N/A
Olympus software	Olympus	N/A
Other		
RNA probe Hic1	ACDBio	464131
RNA probe Crabp1 – C2	ACDBio	474711-C2
RNA probe Prss35 – C3	ACDBio	492611-C3
Rspo3 – C3	ACDBio	402011-C3
GitHub links: https://github.com/BiernaskieLab	This Paper	N/A

RESOURCE AVAILABILITY

Lead Contact

Further information and requests for resources and reagents should be directed to and will be fulfilled by Dr. Jeff Biernaskie (jeff.biernaskie@ucalgary.ca).

Materials Availability

This study did not generate new unique plasmids/reagents.

Data and Code Availability

Single cell RNA-Seq data are available at NCBI GEO (which automatically makes SRA deposit) with the following accession number: GSE108677. Single cell ATAC-Seq data is available at: GSE131600. Single-cell RNA-Seq datasets used for cross-tissue mesenchymal progenitor integration can be access through NCBI GEO with the following accession numbers: GSM2976778 (muscle) and GSM2976778 (heart). Single-cell datasets can be further explored freely at http://biernaskielab.ca/wound_atlas or http://biernaskielab.com/wound_atlas. Associated analysis scripts and raw files is available at: https://github.com/BiernaskieLab/Rodent_Wound.

EXPERIMENTAL MODEL AND SUBJECT DETAILS

Mice

All procedures received prior approval from the University of Calgary Health Sciences Animal Care Committee and all experiments were completed in accordance with the Canadian Council of Animal Care guidelines. All fate mapping experiments used adult α -SMA^{CreERT2};Rosa^{YFP} mice (referred to as “ α SMA-YFP”) (Rahmani et al., 2014) or $Hic1^{CreERT2};Rosa^{tdTomato}$ mice (referred to as “ $Hic1$ -tdTomato”) the generation of which are described elsewhere (Scott et al., 2019). Cre-recombination was initiated with two intraperitoneal (i.p.) injections of 4-hydroxy-tamoxifen (4-OHT; 0,2 mg in sterile sunflower oil, Sigma-Aldrich) at postnatal day (P) 3 and 4. Excision wounds were done 3-4 weeks later. For cell transplant experiments, 6-week-old nude mice (Nu/Nu; Charles River) were used as recipients. $aSMA^{CreERT2};Rosa^{tdTomato}Hic1^{flox/flox}$ (referred to as $Hic1^{flox/flox}$) and their littermates control $aSMA^{CreERT2};Rosa^{tdTomato}Hic1^{WT/WT}$ (referred to as $Hic1^{wt/wt}$) mice were used for the conditional KO of $Hic1$ in myofibroblasts.

METHOD DETAILS

Wound-Induced Hair follicle Neogenesis (WIHN) assay

Full-thickness excision wounds were performed on mice treated with analgesic Meloxicam (Metacam®, 25 mg/kg reconstituted in 100 μ L of sterile saline) subcutaneously and anesthetized using isoflurane (5% induction; 3% maintenance). Full-thickness square excisions (≥ 1.5 cm diameter) were made on the mid-dorsal skin and analgesia (25 mg/kg Metacam® reconstituted in 100 μ L of sterile saline) was provided subcutaneously 24 h post-wound. Wounds were left to heal, and healed skin was harvested between 10 to 28 days post-wound. Neogenic HF were quantified by whole-mount imaging using a V5 Slide Scanner (Olympus Life Science).

Histology, immunofluorescence staining and image analysis

Skin was excised, fixed in 2% paraformaldehyde at 4°C for 48 hr and subsequently snap frozen in OCT compound (Sakura) and then cryosectioned at 50 μ m thickness. (Leica Biosystems). The incorporation of YFP⁺ or tTomato⁺ cells into the DP and DS of neogenic HF in each transgenic strain was quantified for each time point (n = 3-6 mice per time point).

For immunostaining, the following primary antibodies were used: rabbit anti-keratin 14 (1:1200; Covance), rabbit anti-keratin 5 (1:500; Covance), goat anti-ITG α 8 and anti-ITG α 9 (both 1:100, R&D Systems), rat anti-CD200 (Abcam, 1:200), Anti-CD133 Alexa Fluor 488 conjugated (Sigma, 1:200), chicken anti-GFP (1:500; Millipore), rabbit anti-versican (1:200; Millipore), goat anti-Sox18 (1:50; Santa Cruz Biotechnology), goat anti-P-Cadherin (1:150; R&D Systems), rat anti-Ki-67 (1:100; Dako), rabbit anti-Lef1 (1:50, Cell Signaling), goat CD26 (1:20; R&D Systems), goat integrin β 1/CD29 (1:100; R&D Systems), rat Sca-1 (1:50; Abcam), goat PDGFR α (1:20; R&D Systems), and rat CD31 (1:200; Acris antibodies), FABP4 (1:100; R&D Systems). Corresponding Alexa-conjugated secondary antibodies were used for visualization (1:1000; Life Technologies). Nuclei were labeled with Hoechst dye (1:500; Sigma). Images were captured using a Leica SP8 spectral confocal microscope. Z stacks of all images were projected into a single image and the full drop was digitally reconstructed by stitching the different image projections using the Leica Software. Images are tiled and stitched with Leica Software.

Cell isolation and ex-vivo HF formation assay

We used the “patch” hair follicle formation assay (Zheng et al., 2005; Biernaskie et al., 2009) to assess the capacity of prospectively isolated dermal populations to stimulate new HF formation. Populations included: 1) *Hic1*-lineage cells associated with the HF (*Hic1*:tdT⁺ CD133⁺/ITG α 9⁺ ITG α 8⁺/CD200⁺), 2) non-follicular *Hic1*-lineage progenitors (*Hic1*:tdT⁺ CD133⁻ ITG α 9⁻ ITG α 8⁻ and CD200⁻) and 3) non-follicular *Hic1*:tdT⁻ CD133⁻ CD133⁻ ITG α 9⁻ ITG α 8⁻ and CD200⁻). Isolation of dermal cells was done using a FACSAria III cell sorter (BD Biosciences). Each population was combined with epithelial aggregates extracted from back skin of newborn C57BL/6 mice (P0). Dorsal skin was floated on 1 mg/mL dispase for 30 min at 37°C in order to separate the dermis from the epidermis. The dermis was discarded, and the epidermis was transferred to a plate containing 0.25% trypsin (without EDTA) for 3–4 min at 37°C. To inactivate the enzyme, 10% FBS was added. The epidermal sheet was then gently scraped with a scalpel blade. Liberated epithelial cells were transferred to a 15 mL tube and centrifuged to 300 g for 3 minutes and resuspended in DMEM. For each graft, 10,000 epithelial aggregates were combined with each dermal population. Cells were subcutaneously injected under the back skin of adult male nude mice. After 14 days, grafts were harvested and the number of HFs containing Tomato⁺ mesenchyme (with contribution to both DP and DS) within each graft were quantified (n = 3 biological replicate experiments, with a minimum of 3–6 grafts per population).

Single-cell RNA-Seq library construction

To isolate cells comprising wound neoderms, we created small (8 mm diameter) and large (1.5 cm diameter) full-thickness wounds on gender-matched *Hic1*-tdTomato⁺ mice treated with tamoxifen as pups (P4–5). We FACS collected viable *Hic1*-tdTomato⁺ and ⁻ cells from pooled wound tissues (n = 2 female mice per sample) and captured five cell populations: 1) cells in Small Wound D8 (SWD8), 2) SWD14, 3) cells in Large Wound Periphery at D14, 4) cells in Large Wound Center at D14, and 5) cells in uninjured P28 skin. All five samples were processed according to 10X Genomics ChromiumTM Single Cell 3' Reagent Guidelines v2 Chemistry as per the manufacturer's protocol. Quality control and cDNA quantification was performed using Agilent High Sensitivity DNA Kit. Sequencing was performed first using Illumina MiSeq SR50 to approximate the number of recovered cells in each sample. We recovered 1963, 4061, 3776, 2604, and 3293 cells for Samples 1–5, respectively, with an estimated doublet rate of \approx 3%. Based on this, we determined lane distributions for sequencing using Illumina HiSeq 4000 PE (75 bp paired end reads) with a targeted sequencing depth of \sim 115,000 reads/cell. A custom reference genome was generated by appending the tdTomato sequence to the mm10 reference genome and running *cellranger mkref* (Scott et al., 2019). Alignment to the modified reference genome was performed with *cellranger count* (10X Genomics) and libraries were aggregated using *cellranger aggr* (with mapped normalization). The resulting gene-barcode matrix was imported into Seurat v.2.3 (Satija et al., 2015) for quality control, dimensionality reduction, cell clustering, and differential expression analysis. Cell cluster dendrograms were generated using the *PlotClusterTree* function in Seurat v.2.3. Unsupervised clustering was done with original Louvain algorithm using *FindNeighbors* and *FindClusters* functions in Seurat v.2.3. Assignment of cell clusters to wound regions was based either on percent sample composition (classified as being enriched for one sample type if > 70% of fibroblasts in that cluster originated from one sample; Figures 4D–4F) or based on expression of spatially validated marker genes (i.e., *Crabp1* and *Prss35* marking LWC Upper dermal fibroblasts versus *Mest*, *Dlk1* and *Sca1*/Ly6a marking LWC Lower dermal fibroblasts; Figures 4H–4J). Clustering trees were generated using *clustree* v.0.4.2 to visualize and evaluate fibroblast clusterings at multiple resolutions (Zappia and Oshlack, 2018). Additional details regarding analytics are available at: https://github.com/BiernaskieLab/Rodent_Wound. Gene expression signatures were calculated using the *FindMarkers* function in Seurat using the “negbinom” test by looking at genes detected in a minimum of 10% of cells in populations compared. Heatmap plotting top marker genes were generated using the *DoHeatmap* function with thematic modifications using *ggplot2* v.3.1.1. Integration of scRNA-seq datasets capturing resident *Hic1*-lineage progenitors within undamaged heart (GSM4216418), skeletal muscle (GSM2976778), and skin (GSM2910020, this study) was performed using Mutual Nearest Neighbors (MNNs)-based anchoring strategy implemented in Seurat v3 (Stuart et al., 2019). To identify intercellular communication, web-interface of CellPhoneDB v.1 (CellPhoneDB.org) was used to statistically predict receptor–ligand pairs (for > 10% of cells in a cluster expressing a gene, P value 0.05, 10 statistical iterations) between cell types/states defined in Seurat.

Gene Regulatory Network analysis

Single cell regulatory network inference and clustering (SCENIC) (Aibar et al., 2017) was used to infer transcription factor networks active using scRNA-Seq data. Analysis was performed using default and recommended parameters as directed on the SCENIC

vignette (<https://github.com/aertslab/SCENIC>) using the mm9 RcisTarget database. Kernel density line histograms showing differential AUC score distribution across conditions were plotted with ggplot2 v.3.1.1 using the regulon activity matrix ('3.4_regulonAUC.Rds', an output of the SCENIC workflow) in which columns represent cells and rows the AUC regulon activity. Fold-change (FC) difference between median AUC values was calculated and the highest changed TFs were plotted (Figures 5A–5C). Histograms for the remaining TFs can be queried at http://www.biernaskielab.ca/wound_atlas/.

Single-cell ATAC-Seq

To isolate nuclei for use with the 10x Chromium Next GEM Single Cell ATAC v1 workflow, we pooled 50,000 cells from central domains of large wound (n = 3 females) into 100 μ L of chilled Lysis Buffer and incubated for 15–17 minutes on ice according to the Demonstrated Protocol (10x Genomics; <https://support.10xgenomics.com/single-cell-atac>) to achieve > 95% lysis without nuclear blebbing. Nuclei quantification was performed using a CountessTM II Automated Cell Counter (ThermoFisher) and 5,000 nuclei were targeted for transposition and capture using 10x Chromium Chip E. ScATAC-seq libraries were prepared according to the Chromium Single Cell ATAC Reagent Kits User Guide (10x Genomics; CG000168 Rev B). Sequencing was performed using Illumina HiSeq 4000 PE 100bp where ~1,600 cells with 10,364 median fragments per cell (~80% sequencing saturation) were recovered. Cellranger-atac pipeline (version 1.1.0) was used to generate FASTQs and perform preliminary ATAC analysis including read filtering, genome alignment, and barcode counting. Pseudo-bulk ATAC profiles comparing *Pdgfra*⁺ *Crabp1*⁺ (inductive) versus *Pdgfra*⁺ *Crabp1*⁻ (non-inductive) fibroblasts were generated using rulesets joined by logical operators as presented in Loupe Browser ATAC Tutorial (<https://support.10xgenomics.com/single-cell-atac/software/visualization/latest/tutorial-cellsubtypes>). Raw Loupe ATAC file and barcodes assigned to *Pdgfra*⁺ *Crabp1*⁺ and *Pdgfra*⁺ *Crabp1*⁻ groups can be accessed through: https://github.com/BiernaskieLab/Rodent_Wound/tree/master/single-cell_RNA_ATAC_Integration_Large_Wound/Crabp1PosNeg_Loupe_analysis_files. Seurat v3 was used to co-embed scATAC and scRNA datasets by projecting RNA cluster labels onto ATAC dataset for cells that received > 0.5 Prediction Score. Cicero v.1.3.1 was used to calculate co-accessibility scores and predict cis-regulatory interactions (Pliner et al., 2018). Seurat v3 was used to co-embed scATAC and scRNA datasets by projecting RNA cluster labels onto ATAC dataset for cells that received > 0.5 Prediction Score. To visualize “pseudo bulk” profiles of integrated clusters, barcodes and their corresponding labels were imported to Loupe Cell Browser (10X Genomics, v. 3.1.0) using ‘Import Categories’ option. Feature comparison for motifs, peaks, promoter sums, and visualization using cut site tracks were generated from this integrated dataset in Loupe Cell Browser.

Fluorescence In Situ Hybridization (RNAScope)

Skin tissue were collected, fixed and stored as mentioned above. RNAScope 2.0 HD Detection kit was used (ACDBio) for *in situ* hybridization according to manufacturer protocol. The sections were dried for 10 min at room temperature (RT) and then washed with 1X PBS for 5 min to remove excess OCT. The tissue was then incubated in target retrieval (5min, 99°C) and then subsequently washed in distilled water (3x) for 1min each at RT. The tissue was washed in 100% ethanol for 15–20 s and then left to dry. Sections were permeabilized using protease 4 (ACDBio) (40 min, 40°C). Following permeabilization, the tissue was washed with distilled water (3x) for 3 min each. RNA scope probes acclimated to RT were then added to the tissue sections and incubated for 2 hr at 40°C. The C2 and C3 probes were diluted in C1 probe at a 1:50 dilution. Following the incubation, tissue was washed with 1X wash buffer for 2 min twice at RT. The tissue was subsequently incubated and washed as such: AMP1 (30 min, 40°C), washed with 1X wash buffer twice (2 min, RT), incubated in AMP2 (15 min, 40°C), washed with 1X wash buffer twice (2 min, RT), incubated in AMP3 (30 min, 40°C), washed with 1X wash buffer twice for (2 min, RT), incubated in AMP4 (15 min, 40°C), washed with 1X wash buffer twice for (2 min, RT), and finally incubated in Hoechst 33258 (Sigma-Aldrich) (20 min, RT). Slides were mounted with fluorescent medium and left overnight to dry.

Topical application of candidate compounds

Runx1 inhibitor (Ro 5-3335, Tocris Bioscience), all-trans Retinoic Acid agonist (0695, Tocris Bioscience), and Retinoic Acid antagonist BMS 493 (B6688, Sigma) dissolved in 100 μ L of DMSO gel (Medivet, USA) at 100 μ M were applied topically onto large wounds at 2, 4, 6, 8, 10, 12, and 14 days post-wound. Wounds were harvested 28 days post-wound and number of neogenic follicles were counted from each treatment.

Conditional deletion of *Hic1*

To conditionally delete *Hic1* within wound-activated α SMA⁺ myofibroblasts, *Hic1*^{flox/flox} mice were bred with α SMA^{CreERT2}; Rosa^{tdTomato} mice to generate α SMA^{CreERT2}; Rosa^{tdTomato}; *Hic1*^{WT/WT} or α SMA^{CreERT2}; Rosa^{tdTomato}; *Hic1*^{flox/flox} mice. Tamoxifen (0.5 mg in 100 μ L i.p.) was administered daily either between 2 to 6 days post-wound or between 12 to 16 days post-wound to assess early- and late-stage impact of *Hic1* deficiency during healing, respectively. Fibroblast density within central and peripheral domains of large wounds after TAM treatment was quantified from 4% PFA-fixed OCT-embedded 50 μ m skin sections harvested 28 days post-wound (n = 6 per group). Density measurements were obtained by counting number of α SMA-tdTomato⁺ cells within a standardized 50 \times 50 μ m field of view from confocal micrographs using Leica Application Suite X (Leica Microsystems).

To delete *Hic1* in isolated dermal progenitors, TAM was applied to $\alpha\text{SMA}^{\text{CreERT2};\text{Rosa}^{\text{tdTomato}}};\text{Hic1}^{\text{WT}/\text{WT}}$ or *Hic1*^{flox/flox} mice and ITGA8⁺/CD200⁺/tdTomato⁺ cells were FACS isolated from p28 backskin. Dermal progenitors were seeded at 3.0×10^5 cells in 48-well plates, grown in standard media until passaging seven days later, and then reseeded at their initial primary density. Spherical colonies were counted.

QUANTIFICATION AND STATISTICAL ANALYSIS

The number of animals used in each study is indicated in the figure legends. Studies were not randomized and investigators were blinded to analyses. For all measurements used in this report, at least three biological and technical replicates were used. All results are given as means \pm SEM. To determine the significance between two groups, comparisons were made using unpaired 2-tailed t tests with Welch's correction. For comparison between multiple groups, one-way ANOVA multiple comparisons and Tukey post hoc tests were employed. All statistical analyses were carried out using GraphPad Prism 7.0 software and a two-tailed P value with 95% confidence interval was acquired. $p < 0.05$ was considered as significant. The following symbols for statistical significance were used throughout the manuscript: * $p < 0.05$; ** $p < 0.01$; *** $p < 0.001$.

ADDITIONAL RESOURCES

Wound Atlas

To enable intuitive exploration of datasets and analyses described, a web browser interface (http://www.biernaskielab.ca/wound_atlas/ or http://biernaskielab.com/wound_atlas) was created using RShiny (v1.1.0), shinyLP (v.1.1.2), and shinythemes (v.1.1.2) packages.